

Switching of band inversion and topological surface states by charge density wave

N. Mitsuishi^{1*}, Y. Sugita¹, M. S. Bahramy^{1, 2}, M. Kamitani¹, T. Sonobe¹, M. Sakano¹,
T. Shimojima², H. Takahashi³, H. Sakai⁴, K. Horiba⁵, H. Kumigashira⁵,
K. Taguchi⁶, K. Miyamoto⁶, T. Okuda⁶, S. Ishiwata³, Y. Motome¹, K. Ishizaka^{1, 2*}

Affiliations

1. Quantum-Phase Electronics Center (QPEC) and Department of Applied Physics, The University of Tokyo, Tokyo 113-8656, Japan.
2. RIKEN Center for Emergent Matter Science (CEMS), Wako 351-0198, Japan.
3. Division of Materials Physics, Graduate School of Engineering Science, Osaka University, Toyonaka, Osaka 560-8531, Japan.
4. Department of Physics, Osaka University, Toyonaka, Osaka 560-0043, Japan.
5. Condensed Matter Research Center and Photon Factory, Institute of Materials Structure Science, High Energy Accelerator Research Organization (KEK), Tsukuba 305-0801, Japan.
6. Hiroshima Synchrotron Radiation Center (HSRC), Hiroshima University, 2-313 Kagamiyama, Higashi-Hiroshima 739-0046, Japan.

Abstract

Topologically nontrivial materials host protected edge states associated with the bulk band inversion through the bulk-edge correspondence. Manipulating such edge states is highly desired for developing new functions and devices practically using their dissipation-less nature and spin-momentum locking. Here we introduce a transition-metal dichalcogenide VTe_2 , that hosts a charge density wave (CDW) coupled with the band inversion involving $\text{V}3d$ and $\text{Te}5p$ orbitals. Spin- and angle-resolved photoemission spectroscopy with first-principles calculations reveal the huge anisotropic modification of the bulk electronic structure by the CDW formation, accompanying the selective disappearance of Dirac-type spin-polarized topological surface states that exist in the normal state. Thorough three dimensional investigation of bulk states indicates that the corresponding band inversion at the Brillouin zone boundary dissolves upon CDW formation, by transforming into anomalous flat bands. Our finding provides a new insight to the topological manipulation of matters by utilizing CDWs' flexible characters to external stimuli.

Main text

Introduction

Since the discovery of topological insulators, a wide variety of topological phases have been intensively developed and established in realistic materials^{1,2}. The upcoming target is to explore the guiding principle toward the manipulation of these topological states. The key to characterize the topological aspect of materials is the band inversion realized by the crossing and anti-crossing of multiple bands with different parities. In bulk materials, the control of band inversion has been mostly done through the tuning of spin-orbit coupling (SOC) by element substitution^{3,4}, with some exceptions on topological crystalline insulators⁵. In the present work, we focus on charge density wave (CDW), *i.e.* the spontaneous modulation of charge density and lattice that adds new periodicity and symmetry

onto the host crystal. In TaS₂, for example, the Star-of-David type CDW superstructure induces the effective narrowing of valence bands thus causing the Mott transition^{6–8}. From this viewpoint, CDW could also modify the band structures that involve the band inversion, and induce topological change. Moreover, it is worth noting that CDW can be flexibly controlled by external stimuli.

The layered transition-metal dichalcogenide (TMDC) has been a well-known system to host a variety of CDWs reflecting its quasi-two dimensionality⁹. Manipulations of CDW states have been intensively investigated and realized, especially in the aforementioned archetypal material TaS₂, by various stimuli, such as pressure⁷, electric field¹⁰, and optical pulse^{11,12}. The feasibility of CDW thus paves the way toward triggering the exotic phase transitions and generating new functions. More recently, there has been increasing interest in SOC effect in TMDC^{13–18}. Especially in tellurides, (Mo,W)Te₂^{14–16} and (Ta,Nb)IrTe₄^{17,18} are reported to be topological Weyl semimetals. Here, the peculiar quasi-one-dimensional chain-like structures inherent to tellurides, as well as its stronger SOC compared to selenides and sulfides, are essential in realizing the topologically non-trivial states. In this stream, we focus on the telluride CDW material VTe₂, bringing the topological aspect and its manipulation into perspective.

VTe₂ has CdI₂ structure in the high-temperature normal 1T phase, consisting of trigonal layers formed by edge-sharing VTe₆ octahedra (Fig. 1a). With cooling, it undergoes a phase transition to the CDW phase at around 475 K, appearing as a jump in the temperature-dependent resistivity¹⁹. The CDW state exhibits the (3×1×3) superstructure characterized by the double zigzag chains of vanadium atoms (Fig. 1d; hereafter we refer it as 1T'' phase)^{19–21}. This superstructure commonly appears in group-V transition metal ditellurides *M*Te₂ (*M* = V, Nb, Ta)^{20,22}. It has been discussed in terms of CDW induced by the peculiar chemical σ -bonding among *t*_{2g} *d*-orbitals on three adjacent *M* sites, in parallel with other TMDC including TaS₂^{23,24} and purple bronze AMo₆O₁₇ (*A* = Na, K)^{25–27}. Previous band calculation on NbTe₂, on the other hand, implies the importance of Fermi surface nesting and electron-phonon coupling as the origin of CDW with 1T'' lattice distortion²⁸. However, the modifications of

electronic structure by this CDW transition have not been precisely investigated so far. It is worth noting that the contraction of metal-metal bond length ($\Delta a_{\text{max}}/a$) *via* the CDW transition in VTe₂ is fairly large ($\sim 9.1\%$)²⁰ and comparable to that in TaS₂ ($\sim 7.0\%$)²⁹. We also note that the CDW in VTe₂ can be optically manipulated, as reported by recent time-resolved diffraction studies^{30,31}.

In this Article, we investigate the electronic structures of VTe₂, by employing spin- and angle-resolved photoemission spectroscopy (ARPES) and first-principles calculations. We focus on the modifications of the bulk bands through the CDW formation, and its relevance to the Dirac surface states stemming from the topological band inversion. Experimentally it is not easy to perform highly precise ARPES measurement on the normal $1T$ phase of pristine VTe₂ (> 475 K), since such high temperature may cause the sample degradation. Therefore we notice on TiTe₂ showing a simple $1T$ structure down to the lowest temperature³², and develop the single crystalline V_{1-x}Ti_xTe₂ to access both $1T$ and $1T''$ phases at appropriate temperatures. Figure 1f displays the schematic electronic phase diagram of V_xTi_{1-x}Te₂, based on the temperature-dependent ARPES measurements. With increasing Ti, the CDW phase transition becomes gradually suppressed to the lower temperature region (see Supplementary Note 1). For investigating both the normal and CDW phases within a single sample, we synthesized the minimally Ti-doped single crystals ($0.10 \leq x \leq 0.13$) showing the transition just below room temperature ($280 \sim 250$ K). To discuss the electronic structures in momentum space, we introduce the following notation of the Brillouin zones (BZ). In $1T$, the 2-dimensional (3-dimensional) BZ is represented by the hexagonal plane (prism) reflecting the trigonal symmetry (Figs. 1b, c). In $1T''$, the BZ changes into a smaller one of lower symmetry as indicated in Fig. 1e. In this paper, we use the $1T$ BZ notation to present the band structures in $1T$ and $1T''$ in a common fashion. To account for the in-plane anisotropy of vanadium chains that is essential in $1T''$, we define \bar{K}_1 , \bar{K}_2 and \bar{M}_1 , \bar{M}_2 as depicted in Fig. 1e (see Supplementary Note 1 for the details of BZ).

Results and Discussion

Overviewing the electronic structures and modification by CDW

Let us start by briefly overviewing the anisotropic modification of electronic structures from $1T$ to $1T''$ by presenting the ARPES data successfully focused on a CDW single-domain region. Figure 2a shows the ARPES image for the normal state $1T\text{-V}_{0.87}\text{Ti}_{0.13}\text{Te}_2$ taken at 300 K with a He discharge lamp (photon energy $h\nu = 21.2$ eV). We find V-shaped band dispersions along $\bar{K} - \bar{M} - \bar{K}$ that clearly cross the Fermi level (E_F). Looking at the higher binding energy (E_B) region, these V-shaped bands are connected to the Dirac-cone-like bands reminiscent of surface states in topological insulators, with the band crossing (Dirac points) at \bar{M} . The topological character of these Dirac bands will be discussed later. On the other hand, Fig. 2b displays the ARPES results on a single-domain CDW state in $1T''\text{-VTe}_2$ (200 K, synchrotron light $h\nu = 90$ eV). Because of the zigzag type CDW formation, the system now loses the 3-fold rotational symmetry, and the 3 equivalent \bar{M} points in $1T$ turn into one \bar{M}_1 and two \bar{M}_2 . Here, the V-shaped band and Dirac-like bands remain at \bar{M}_1 , whereas at \bar{M}_2 side the unusual flat band is observed and the Dirac-like state is vanished. Thus, the $1T$ - $1T''$ CDW transition induces the huge directional change of electronic structure accompanying the selective disappearance of Dirac-like states. In the following, we discuss these band structures in detail, by comparing with band calculations.

Figures 3a and 3b respectively display the bulk band calculation for the normal state $\text{V}_{0.87}\text{Ti}_{0.13}\text{Te}_2$ along high symmetry lines (Γ -K-M- Γ) and the Fermi surface at $k_z = 0$ (see Supplementary Note 3). They are characterized by the circular and triangular hole Fermi surfaces respectively around Γ and K. The ARPES results on normal state $\text{V}_{0.90}\text{Ti}_{0.10}\text{Te}_2$ (350 K, marked as “#1” in Fig. 1f) are shown in Figs. 3c, d. Here a He discharge lamp ($h\nu = 21.2$ eV) is used as the light source. The black broken curves in Fig. 3c are the guides for the bands plotted by tracking the peaks of the energy/momentum distribution curves (EDCs/MDCs) (see Supplementary Note 4). We find hole-like bands centered at around $\bar{\Gamma}$ and \bar{K} points, in a qualitative agreement with the calculation in Fig. 3a (We note that the tiny electron pocket at Γ is not clearly detected, probably reflecting the finite energy

mismatch of the bands compared to the calculation.). In the EDCs along the $\bar{M} - \bar{K}$ line (Fig. 3d), we can clearly trace a dispersive band that crosses the Fermi level.

To grasp the essential electronic modification *via* the CDW formation, we survey the temperature- and doping-dependent ARPES results (He discharge lamp, $h\nu = 21.2$ eV). Note that the $1T''$ phase inevitably contains the in-plane 120-degree CDW domains reflecting the 3-fold symmetry of $1T$, and usually ARPES measurements include the signals of multiple domains (see Supplementary Note 5). Figures 3e, f respectively show the ARPES image and corresponding EDCs of $V_{0.90}Ti_{0.10}Te_2$ in the CDW $1T''$ phase (multi-domain, 20 K, #2). Comparing with the high temperature $1T$ phase (#1), we notice a very unusual flat band appearing at the binding energy of $0.1 \sim 0.25$ eV as denoted by the red curve in Fig. 3e, spreading over the measured momentum region. This is most well recognized in Fig. 3f as the series of EDC peaks at $E_B \sim 0.2$ eV around the \bar{K}_1/\bar{K}_2 point. The blue broken curve in Fig. 3e, on the other hand, indicates the dispersive band crossing E_F resembling the high temperature normal phase (see Supplementary Note 6 for the detailed temperature-dependence). Such coexistence of flat/dispersive bands results from the mixing of CDW domains. In the pristine $1T''$ -VTe₂ (multi-domain, 15 K, #3) as shown in Figs. 3g and 3h, the similar flat band with slightly different energy and dispersion is more clearly observed (red broken curve), together with the $1T$ -like dispersive band (blue broken curve). The appearance of this anomalous flat band is thus the common signature of the CDW $1T''$ phase, which however is seemingly beyond the simple band folding and gap opening in the Fermi surface nesting scenario. The localized nature of this electronic structure will be discussed later.

Bulk and surface band structures in $1T$ normal phase

Here we introduce the topological aspect that can be relevant to the $1T$ - $1T''$ CDW transition. In the normal $1T$ phase, the band calculation suggests the band inversion involving V3d and Te5p orbitals at around the M and L points. The calculations of $1T$ - $V_{0.87}Ti_{0.13}Te_2$ at several k_z , plotted along the momentum parallel to Γ -M ($k_{\Gamma M}$, see Fig. 4a) are displayed in Fig. 4b. The colors of curves show the

weight of atomic orbitals as depicted by the color-scale (see Supplementary Note 3 for detailed orbital components), whereas the black broken curves are the results without SOC. Focusing on the topmost two bands at M and L, depicted by A and B, we find that their orbital characters of mainly V3d (blue-like, even parity) and Te5 p_x+p_y (red-like, odd parity) get inverted at a certain k_z ($\sim 0.76 \pi/c$). In the corresponding (0 0 1) slab calculation (Fig. 4c), the band spreading around $E - E_F = -0.6$ eV near \bar{M} is recognized, that does not exist in the bulk calculations. It roughly follows the trajectory of the virtual crossing points of bulk bands A and B for no SOC. This should be the surface state topologically protected by the band inversion at $(a^*/2, 0, k_z)$ occurring due to the moderate k_z dispersions of V3d and Te5p bands. Indeed, in the $\bar{K} - \bar{M} - \bar{K}$ direction (Fig. 4d), this surface state shows a Dirac cone-like dispersion connecting bands A and B. Figure 4e shows the ARPES image of normal-state V_{0.90}Ti_{0.10}Te₂ along $\bar{K} - \bar{M} - \bar{K}$ (350 K, $h\nu = 21.2$ eV). By carefully analyzing the EDC/MDC (see Supplementary Note 7), we can indeed quantify the bottom of bulk band A ($E_B \sim 0.30$ eV), the top of bulk band B (~ 0.90 eV), and the crossing point of the surface Dirac cone (DP, ~ 0.66 eV). We note that this bulk band A forms the triangular Fermi surfaces centered at \bar{K} points in the $k_z = 0$ plane, as shown in the Fermi surface image in Fig. 4f (V_{0.87}Ti_{0.13}Te₂, 300 K, $h\nu = 83$ eV).

We further perform the $h\nu$ -dependent ARPES to confirm the two-dimensionality of the Dirac surface states and to clarify the k_z -dependent bulk electronic structure that is relevant to the band inversion. Figures 4h, i, and j display the ARPES images of 1T-V_{0.90}Ti_{0.10}Te₂ near the \bar{M} point (see the red arrow in Fig. 4g), recorded at 320 K with different photon energies, $h\nu = 63, 69$, and 78 eV, respectively corresponding to $k_z \sim 0, \pi/2c$, and π/c . Circle markers with vertical (horizontal) error bars represent the peak positions of EDCs (MDCs) (see Supplementary Note 7). Figure 4k displays the schematic band dispersions overlaid with the experimental peak plots extracted from Figs. 4h-j. Here we find that the bulk bands A and B clearly show the finite k_z -dispersions (respectively larger than 0.1 and 0.4 eV at \bar{M}). As seen in Fig. 4b, this k_z -dispersion is essential for the band inversion at $(a^*/2, 0, k_z)$, the origin of the topological surface state appearing around the \bar{M} point. On the other hand, the

Dirac surface state, that is highlighted by the overlaid orange curves in Fig. 4k, is almost independent of $h\nu$, indicating the two-dimensional nature of the topological surface state.

Bulk and surface band structures in $1T''$ CDW phase

To unambiguously elucidate the anisotropic electronic structures in the CDW $1T''$ phase, here we utilize the small spot size (typically 300 μm) of the synchrotron light beam and separately measure the in-plane CDW domains of VTe_2 (see Supplementary Note 5). Figure 5a shows the Fermi surface image of the single-domain $1T''$ - VTe_2 (200 K, $h\nu = 90$ eV). We find that the two sides of the triangular Fermi surface around \bar{K} observed in the normal $1T$ phase (Fig. 4f) are completely absent in the CDW state, and the remaining one forms the quasi-one-dimensional Fermi surface marked by the red broken curves. Figures 5b and 5d display the ARPES images along representative two cuts (cut #1 and #2 as denoted in Fig. 5a), nearly along $\bar{K}_1 - \bar{M}_1 - \bar{K}_1$ and $\bar{K}_1 - \bar{M}_2 - \bar{K}_2$, respectively. Though they are originally the equivalent momentum cuts in the normal $1T$ phase, distinctive features are clearly observed. Along $\bar{K}_1 - \bar{M}_1 - \bar{K}_1$, there are several bands crossing E_F including the $1T$ -like dispersion (the black broken curve), together with the Dirac-cone like band (the white broken curve) as clearly seen in the MDCs (Fig. 5c). On the other hand, along $\bar{K}_1 - \bar{M}_2 - \bar{K}_2$, the bands crossing E_F as well as the Dirac band completely disappear (see the MDCs in Fig. 5e), and the peculiar flat band (the black broken curve in Fig. 5d) appears around $E_B \sim 0.2$ to 0.3 eV. These indicate that the CDW induces the drastic directional modification of electronic structure.

Here, to confirm the topological nature of the Dirac surface state in VTe_2 , we performed spin-resolved ARPES on a multi-domain sample (see Supplementary Note 8 for the experimental setup). Figure 5f depicts the schematic 2D BZ with CDW multi-domains, together with the measurement region (the red arrow). Figure 5g shows the spin-integrated ARPES image with the peak plots obtained from spin-resolved spectra (15 K, $h\nu = 21$ eV, s polarization). By comparing with the results from the single-domain measurement (Figs. 5b-e), these peaks can be easily assigned to either \bar{M}_1 or \bar{M}_2 side.

The red (blue) and purple (cyan) triangle markers respectively represent the peak positions of spin-up (-down) spectra at \bar{M}_1 and \bar{M}_2 sides. As shown in the spin-resolved spectra in Fig. 5h, the lower branch of the Dirac cone band clearly shows the spin polarization with sign reversal at \bar{M}_1 point (*i.e.* Dirac crossing point), similarly to the topological surface state in the topological insulators. On the other hand, the bulk flat bands around $E_B \sim 0.25$ eV at \bar{M}_2 side indeed show the spin degenerate character. Figure 5i is an expanded viewgraph of spin-resolved spectra near the Fermi level at emission angle $\theta = \pm 4^\circ$. There are slight spin-up/down intensity contrasts just below E_F ($E_B \sim 0.05$ eV), which should be corresponding to the upper branch of the surface Dirac cone band at \bar{M}_1 side.

Similarly to the normal phase, $h\nu$ -dependent ARPES measurement is performed on CDW state VTe₂ (15 K, multi-domain) to clarify the k_z -dependence of electronic structures. Figures 5j, k, and l display the ARPES image near the \bar{M}_1/\bar{M}_2 point (see the red arrow in Fig. 5f), recorded with the photon energies of 54, 61.5, and 69 eV, respectively. Again by comparing with the single-domain measurement, we can assign the peaks to either \bar{M}_1 or \bar{M}_2 side (see Supplementary Note 9). Figures 5m and n respectively show the schematic band dispersions along $\bar{K}_1 - \bar{M}_1 - \bar{K}_1$ and $\bar{K}_1 - \bar{M}_2 - \bar{K}_2$, overlaid with the experimental peak plots extracted from Figs. 5j-l. At the \bar{M}_1 side, the V-shaped band with high intensity clearly shows the finite k_z -dispersion of > 0.2 eV, together with the $h\nu$ -independent Dirac surface state. These are similar to the case of normal 1T phase along $\bar{K} - \bar{M} - \bar{K}$ (Fig. 4k). On the other hand, at the \bar{M}_2 side, the emergent flat band shows negligible k_z -dependence, in contrast to the V-shaped band observed at the \bar{M}_1 side. With this we can conclude that the electronic state at the \bar{M}_2 side has unusually localized nature, which should give rise to the dissolution of the band inversion along k_z direction.

Picture of CDW state based on orbital bonding

To grasp the essential feature of the CDW state, here we introduce the local orbital picture. For simplicity, we adopt an orthogonal octahedral XYZ coordination by considering the VTe₆ octahedron

as shown in Fig. 6a, and focus on V3d t_{2g} (d_{xy} , d_{yz} , d_{zx}) orbitals that dominate the density of states near E_F (see Supplementary Note 10). Note that this is different from the global xyz setting adopted in Fig. 4a, where z corresponds to the stacking direction. Here we choose Z as the V-Te bond direction that is perpendicular to the vanadium's chain direction b_m .

Figure 6b shows the calculated partial density of states (PDOS) for vanadium d_{xy} , d_{yz} , and d_{zx} orbitals. In $1T$ (Fig. 6b left), they are naturally degenerate reflecting the trigonal symmetry. In $1T''$ (Fig. 6b right), on the other hand, d_{yz}/d_{zx} and d_{xy} orbitals have strikingly different distributions. We can classify the PDOS for $1T''$ into three major parts, lower, middle, and upper, respectively lying around $E_B \sim 0.4$, -0.5 , and -1.3 eV. They are indicative of bonding (B), nonbonding (NB), and antibonding (AB) bands, arising from the trimerization-like displacements of three adjacent vanadium atoms formed by the σ -bonding of d_{yz}/d_{zx} orbitals^{23,33}, as marked by the pink oval in Fig. 6a for d_{yz} . Through the d_{yz}/d_{zx} trimerization, the remaining d_{xy} stays relatively intact, thus its PDOS mostly contributes to the middle band. Here, the d_{yz}/d_{zx} bonding band makes a peak in PDOS at around $E_B \sim 0.3$ eV, corresponding to the flat bands lying around $\bar{\Gamma} - \bar{K}_2 - \bar{M}_2$ (see Supplementary Note 10 for the band dispersions). The experimentally observed flat band in Fig. 5d should be thus reflecting the localized nature of d_{yz}/d_{zx} trimers.

Such orbital bonding picture is also useful for the intuitive understanding of Fermi surfaces at BZ boundary. Figure 6c depicts the schematics of the Fermi surfaces with the locations of the Dirac crossing points (yellow circle markers at \bar{M} points). According to the calculation in $1T$, the three sides of the triangular Fermi surface mainly consist of d_{yz} , d_{zx} and d_{xy} orbitals, respectively (see Supplementary Note 10). This can be regarded as the virtual combination of one-dimensional Fermi surfaces formed by the σ -bonding of d_{yz} , d_{zx} and d_{xy} orbitals, raised as the basic concept of the hidden nesting scenario in CdI₂-type TMDC²³ and purple bronzes AMo_6O_{17} ($A = Na, K$)²⁵⁻²⁷. In the CDW $1T''$ phase, the two sides of the Fermi surfaces composed of d_{yz}/d_{zx} orbitals (\bar{M}_2 sides) turn into the localized flat bands as a consequence of the vanadium trimerization, while the one composed of d_{xy}

remains intact. This explains the quasi-2D to quasi-1D change of the triangular Fermi surface at BZ boundary as obtained in the present result.

Switching of band inversion and topological surface states by CDW

Figure 6d summarizes the observed anisotropic reconstruction of the bulk and topological surface states occurring around the BZ boundaries by CDW formation. As discussed, the band structures observed in the normal $1T$ phase are basically in a good agreement with the calculation, indicating the triangular hole Fermi surfaces around the \bar{K} points. At \bar{M} points, the Dirac-type topological surface states exist in addition to the V-shaped bulk bands. It is well explained by the band inversion of $V3d$ and $Te5p$ orbitals occurring at $(a^*/2, 0, k_z)$, due to the finite k_z dispersion as also experimentally confirmed (Fig. 4k). In the CDW state, on the other hand, drastic changes show up in the electronic structures. The originally triangular hole Fermi surface around the \bar{K} point loses its two sides, and the remaining one forms the one-dimensional-like Fermi surface at the \bar{M}_1 side. We note that this corresponds to the vanadium zigzag chain direction. At the \bar{M}_2 side, the V-shaped bulk band transforms into the flat band at around $E_B \sim 0.25$ eV, reflecting the vanadium trimerization. The Dirac surface state maintains at \bar{M}_1 , but is completely absent at \bar{M}_2 . The disappearance of the Dirac surface state can be described by the dissolution of the band inversion at \bar{M}_2 , where the k_z -dependence of the bulk state is lost due to the flat band formation (Fig. 5n), in contrast to the \bar{M}_1 side (Fig. 5m). Thus, in this system, the CDW accompanying the metal trimerization plays a crucial role on selectively switching off the band inversion and corresponding topological surface state.

Here we attempt an argument on the band inversion in association with CDW based on the change in crystal symmetry. In the high-temperature $1T$ phase ($P\bar{3}m1$), as mentioned, the Dirac cones appear at the \bar{M} points, due to the band inversions involving the $Te5p$ and $V3d$ orbitals occurring along M-L lines. Here, the M-L line resides in a mirror plane, which prohibits the hybridization between the band consisting of $Te5p$ anti-bonding orbitals (odd with respect to the mirror plane) and

that derived from the predominantly $V3d$ with finite $Te5p$ bonding orbitals (even with respect to the mirror plane), without the help of SOC. Eventually, the non-relativistic bands cross at $k_z \sim 0.76 \pi/c$ along M-L depicted as the broken curves in Fig. 4b, thus causing the band inversion, due to the k_z dependent energy eigenvalues. Only by the SOC, they get mixed and make a gap (~ 200 meV) around the crossing point. In the low-temperature $1T'$ phase ($C2/m$), on the other hand, while the \bar{M}_1 point keeps the similar situation with the \bar{M} point in high- T phase, \bar{M}_2 no longer resides in the mirror plane. At \bar{M}_2 , the $V3d$ and $Te5p$ (bonding, antibonding) can now significantly mix and form the well hybridized flat band with no k_z dependence, leading to the disappearance of the band inversion. This can be also confirmed by evaluating the orbital components in our bulk calculation (see Supplementary note 11). It indicates the significant dyz/dzx - p_z hybridization (here X, Y, Z represents the octahedral setting, see Fig. 6a) forming the flat band at the binding energy of ~ 0.4 eV. In contrast, the mirror plane remains for $\bar{\Gamma} - \bar{M}_1$, thus the band inversion and the related Dirac surface state can sustain.

Finally, we would like to mention that the topological character of materials should be determined by considering the detailed band structures for the whole system and quantifying the Berry curvature and topological invariants (Z_2 index, (spin) Chern number, etc). The difficulty in the present case, however, is that the accuracy of the band calculation on $1T'$ phase is still insufficient. Though the qualitative features (such as the quasi-one-dimensional Fermi surface and the flat band formation) are quite well reproduced (see Supplementary Note 12 for the band unfolding calculation), the detailed band structures including their relative energy positions are not in good enough agreement. This makes it difficult to fully discuss the topology which sharply depends on the crossings of band energy levels, particularly on its modification across the CDW transition. In this viewpoint, we would rather like to stress that our present results and microscopic analysis are offering one way to pursue the topological character of a complex material that is still difficult to predict.

Conclusion

We precisely clarified the bulk and surface electronic structures of (V,Ti)Te₂ by utilizing ARPES and first-principles calculation. We revealed that the strongly orbital-dependent reconstruction of the electronic structures occurs through the CDW formation, giving rise to the topological change in particular bands. Considering that CDWs are often flexible to external stimuli^{7,10–12}, we can also expect to manipulate the CDW-coupled topological state. The effect of thinning the crystals down to atomic thickness is also worth investigating, which may give rise to hidden CDW states¹⁰ and electronic phase transitions^{34,35}. The combination of CDW ordering and topological aspects may lead to the new stage of manipulating the quantum materials.

Methods

Sample preparation.

High-quality single crystals of $V_{1-x}Ti_xTe_2$ were grown by the chemical vapor transport (CVT) method with $TeCl_4$ as a transport agent. Temperatures for source and growth zones are respectively set up as 600 °C and 550 °C. The Ti concentrations (x) were characterized by energy dispersive x-ray spectrometry (EDX) measurements. To access both $1T$ and $1T''$ phases, we used $V_{0.90}Ti_{0.10}Te_2$, $V_{0.87}Ti_{0.13}Te_2$, and VTe_2 samples with the transition temperature of ~ 280 K, ~ 250 K and ~ 475 K, respectively.

ARPES measurements.

ARPES measurements were made at the Department of Applied Physics, The University of Tokyo, using a VUV5000 He-discharge lamp and a VG-Scienta R4000 electron analyzer. The photon energy and the energy resolution are set to 21.2 eV ($HeI\alpha$) and 15 meV. The spot size of measurements was $\sim 2 \times 2$ mm². The data in Figs. 2a, 3c-h and 4e were obtained with this condition.

Photon-energy-dependent and domain-selective ARPES measurements were conducted at BL28A in Photon Factory (KEK) by using a system equipped with a Scienta SES2002 electron analyzer. Photon-energy-dependent measurements on $1T$ - $V_{0.90}Ti_{0.10}Te_2$ and $1T''$ - VTe_2 were performed respectively using circular and s polarized light ($h\nu = 45 \sim 90$ eV). The energy resolution was set to 30 meV. The relation between the incident light energy and the detected k_z value is estimated from the experimentally obtained work function (~ 3.7 eV) and inner potential (~ 8.8 eV). The data in Figs. 4h-j and 5j-l were obtained in this condition. Domain-selective measurements on $1T''$ - VTe_2 were performed at 200 K using a 90 eV circularly polarized light with a spot size of $\sim 100 \times 300$ μm^2 . The energy resolution was set to 50 meV. The data in Figs. 5b and 5d were obtained from the different in-plane domains of a single sample, by translating the sample without changing its orientation. The Fermi

surface images in Figs. 4f and 5a were also obtained with this instrument.

Spin-resolved ARPES measurements were performed at Efficient SPin Resolved SpectroScOpy (ESPRESSO) end station attached to the APPLE-II-type variable polarization undulator beamline (BL-9B) at the Hiroshima Synchrotron Radiation Center (HSRC)³⁶. The analyzer of this system consists of two sets of very-low-energy electron diffraction (VLEED) spin detectors, combined with a hemispherical electron analyzer (VG-Scienta R4000). Measurements of $1T''$ -VTe₂ were performed using a *s*-polarized 21 eV light at 15 K. In the spin resolved measurements, we set the energy and angle resolutions to 120 meV and ± 1.5 deg, respectively. We adopted the Sherman function $S_{\text{eff}} = 0.25$ for analyzing the obtained data. The data in Figs. 5g-i were obtained with this condition.

In all the ARPES experiments, samples were cleaved at room temperature *in-situ*, and the vacuum level was better than 5×10^{-10} Torr through the measurements. The Fermi level of the samples were referenced to that of polycrystalline golds electrically connected to the samples.

Band calculations.

The relativistic electronic structure of $1T$ -V_{0.87}Ti_{0.13}Te₂ was calculated within the density functional theory (DFT) using the Perdew-Burke-Ernzerhof (PBE) exchange-correlation functional corrected by the semilocal Tran-Blaha-modified Becke-Johnson potential, as implemented in the WIEN2k package³⁷. The effect of Ti doping was treated within the virtual crystal approximation³⁸. The BZ was sampled by a $20 \times 20 \times 20$ *k*-mesh and the muffin-tin radius R_{MT} for all atoms was chosen such that its product with the maximum modulus of reciprocal vectors K_{max} becomes $R_{\text{MT}}K_{\text{max}} = 7.0$. To describe the surface electronic structure, the bulk DFT calculations were downfolded using maximally localized Wannier functions^{39,40} composed of V3*d* and Te5*p* orbitals, and the resulting 22-band tight-binding transfer integrals implemented within a 200-unit supercell. For the pristine $1T$ - and $1T''$ -VTe₂, the DFT electronic structure calculations were carried out by OpenMX code (<http://www.openmx-square.org/>), using the PBE exchange-correlation functional and a fully relativistic *j*-dependent pseudopotentials.

We adopted and fixed the crystalline structures of $1T$ - and $1T'$ -VTe₂ reported in ref. ^{20,41} and sampled the corresponding BZ by a $8 \times 8 \times 8$ \mathbf{k} -mesh.

Data Availability

The datasets that support the findings of the current study are available from the corresponding author on reasonable request.

References

1. Fu, L. & Kane, C. L. Topological insulators with inversion symmetry. *Phys. Rev. B - Condens. Matter Mater. Phys.* **76**, 045302 (2007).
2. Hasan, M. Z. & Kane, C. L. Colloquium: Topological insulators. *Rev. Mod. Phys.* **82**, 3045–3067 (2010).
3. Xu, S. *et al.* Topological phase transition and texture inversion in a tunable topological insulator. *Science*. **332**, 560–565 (2011).
4. Sato, T. *et al.* Unexpected mass acquisition of Dirac fermions at the quantum phase transition of a topological insulator. *Nat. Phys.* **7**, 840–844 (2011).
5. Dziawa, P. *et al.* Topological crystalline insulator states in $\text{Pb}_{1-x}\text{Sn}_x\text{Se}$. *Nat. Mater.* **11**, 1023–1027 (2012).
6. Rossnagel, K. & Smith, N. V. Spin-orbit coupling in the band structure of reconstructed 1T-TaS₂. *Phys. Rev. B* **73**, 073106 (2006).
7. Sipoş, B. *et al.* From Mott state to superconductivity in 1T-TaS₂. *Nat. Mater.* **7**, 960–965 (2008).
8. Rossnagel, K. On the origin of charge-density waves in select layered transition-metal dichalcogenides. *J. Phys. Condens. Matter* **23**, 213001 (2011).
9. Wilson, J. A. & Yoffe, A. D. The transition metal dichalcogenides discussion and interpretation of the observed optical, electrical and structural properties. *Adv. Phys.* **18**, 193–335 (1969).
10. Yoshida, M. *et al.* Controlling charge-density-wave states in nano-thick crystals of 1T-TaS₂. *Sci. Rep.* **4**, 7302 (2014).
11. Stojchevska, L. *et al.* Ultrafast switching to a stable hidden quantum state in an electronic crystal. *Science*. **344**, 177–180 (2014).
12. Sun, K. *et al.* Hidden CDW states and insulator-to-metal transition after a pulsed femtosecond laser excitation in layered chalcogenide 1T-TaS_{2-x}Se_x. *Sci. Adv.* **4**, eaas9660 (2018).
13. Bahramy, M. S. *et al.* Ubiquitous formation of bulk Dirac cones and topological surface states from a single orbital manifold in transition-metal dichalcogenides. *Nat. Mater.* **17**, 21–28 (2018).
14. Sun, Y., Wu, S. C., Ali, M. N., Felser, C. & Yan, B. Prediction of Weyl semimetal in orthorhombic MoTe₂. *Phys. Rev. B* **92**, 161107 (2015).
15. Soluyanov, A. A. *et al.* Type-II Weyl semimetals. *Nature* **527**, 495–498 (2015).
16. Sakano, M. *et al.* Observation of spin-polarized bands and domain-dependent Fermi arcs in polar Weyl semimetal MoTe₂. *Phys. Rev. B* **95**, 121101 (2017).
17. Haubold, E. *et al.* Experimental realization of type-II Weyl state in noncentrosymmetric TaIrTe₄. *Phys. Rev. B* **95**, 241108 (2017).
18. Li, L. *et al.* Ternary Weyl semimetal NbIrTe₄ proposed from first-principles calculation. *Phys. Rev. B* **96**, 024106 (2017).
19. Ohtani, T., Hayashi, K., Nakahira, M. & Nozaki, H. Phase transition in $\text{V}_{1+x}\text{Te}_2$ ($0.04 \leq x \leq 0.11$). *Solid State Commun.* **40**, 629–631 (1981).
20. Bronsema, K. D., Bus, G. W. & Wieggers, G. A. The crystal structure of vanadium ditelluride,

$V_{1+x}Te_2$. *J. Solid State Chem.* **53**, 415–421 (1984).

21. Ikeura, K., Sakai, H., Bahramy, M. S. & Ishiwata, S. Rich structural phase diagram and thermoelectric properties of layered tellurides $Mo_{1-x}Nb_xTe_2$. *APL Mater.* **3**, 041514 (2015).
22. Brown, B. E. The crystal structures of $NbTe_2$ and $TaTe_2$. *Acta Crystallogr.* **20**, 264–267 (1966).
23. Whangbo, M. H. & Canadell, E. Analogies between the concepts of molecular chemistry and solid-state physics concerning structural instabilities. Electronic origin of the structural modulations in layered transition-metal dichalcogenides. *J. Am. Chem. Soc.* **114**, 9587–9600 (1992).
24. Canadell, E., Jobic, S., Phane, Brec, R., Rouxel, J. & Whangbo, M. H. Importance of short interlayer $Te \cdots Te$ contacts for the structural distortions and physical properties of CdI_2 -type layered transition-metal ditellurides. *J. Solid State Chem.* **99**, 189–199 (1992).
25. M.-H. Whangbo, E. Canadell, P. Foury, J.-P. P. Hidden Fermi Surface Nesting and Charge Density Wave Instability in Low-Dimensional Metals. *Science.* **252**, 96–98 (1991).
26. Mou, D. *et al.* Discovery of an Unconventional Charge Density Wave at the Surface of $K_{0.9}Mo_6O_{17}$. *Phys. Rev. Lett.* **116**, 196401 (2016).
27. Su, L., Hsu, C. H., Lin, H. & Pereira, V. M. Charge Density Waves and the Hidden Nesting of Purple Bronze $K_{0.9}Mo_6O_{17}$. *Phys. Rev. Lett.* **118**, 257601 (2017).
28. Battaglia, C. *et al.* Fermi-surface-induced lattice distortion in $NbTe_2$. *Phys. Rev. B* **72**, 195114 (2005).
29. Brouwer, R. & Jellinek, F. The low-temperature superstructures of 1T- $TaSe_2$ and 2H- $TaSe_2$. *Phys. B+C* **99**, 51–55 (1980).
30. Nakamura, A. *et al.* Evaluation of photo-induced shear strain in monoclinic VTe_2 by ultrafast electron diffraction. *Appl. Phys. Express* **11**, 092601 (2018).
31. Nakamura, A. *et al.* Nanoscale imaging of unusual photo-acoustic waves in thin flake VTe_2 . *Submitted* (<https://arxiv.org/abs/2003.05596>).
32. Koike, Y., Okamura, M., Nakanomyo, T. & Fukase, T. Log T dependence of resistivity and negative magnetoresistance in the layered compound $TiTe_2$. *J. Phys. Soc. Japan* **52**, 597–604 (1983).
33. Katayama, N. *et al.* Large entropy change derived from orbitally assisted three-centered two-electron σ bond formation in a metallic $Li_{0.33}VS_2$. *Phys. Rev. B* **98**, 081104 (2018).
34. Fei, Z. *et al.* Edge conduction in monolayer WTe_2 . *Nat. Phys.* **13**, 677–682 (2017).
35. Chen, P. *et al.* Emergence of charge density waves and a pseudogap in single-layer $TiTe_2$. *Nat. Commun.* **8**, 516 (2017).
36. Okuda, T. *et al.* Efficient spin resolved spectroscopy observation machine at Hiroshima Synchrotron Radiation Center. *Rev. Sci. Instrum.* **82**, 103302 (2011).
37. Blaha, P. *et al.* wien2k package, Version 13.1. (2013).
38. Bellaiche, L. & Vanderbilt, D. Virtual crystal approximation revisited: Application to dielectric and piezoelectric properties of perovskites. *Phys. Rev. B - Condens. Matter Mater. Phys.* **61**,

7877–7882 (2000).

- 39. Souza, I., Marzari, N. & Vanderbilt, D. Maximally localized Wannier functions for entangled energy bands. *Phys. Rev. B* **65**, 035109 (2002).
- 40. Mostofi, A. A. *et al.* wannier90: A tool for obtaining maximally-localised Wannier functions. *Comput. Phys. Commun.* **178**, 685–699 (2008).
- 41. Terzieff, P., Ipser, H. & Wachtel, E. Transition metal-chalcogen systems IX: The vanadium-tellurium system - phase diagram and magnetic properties. *J. Less-Common Met.* **119**, 1–12 (1986).

Acknowledgements

The authors thank N. Katayama for fruitful discussions. We also acknowledge H. Masuda and A. H. Mayo for their assistance with EDX measurements. N.M. acknowledges the support by the Program for Leading Graduate Schools (ALPS). Y.S., M.K. and T.So acknowledge the supports by the Program for Leading Graduate Schools (MERIT). Y.S. and T.So acknowledge the supports by Japan Society for the Promotion of Science through a research fellowship for young scientists. The spin-resolved ARPES experiments were performed under HSRC Proposals Nos. 16AG050 and 16BG040. This work was partly supported by CREST, JST (No. JP-MJCR16F1, No. JPMJCR16F2).

Author contributions

N.M., T.So., M.S., T. Sh. and K.I. carried out (S)ARPES measurements. M.K., H.T., H.S. and S.I. carried out the crystal growth and characterization. M.S.B., Y.S. and Y.M. carried out the calculations. K.H. and H.K. shared the ARPES infrastructure at Photon Factory, KEK, and assisted with measurements. K.T., K. M. and T.O. shared the SARPES infrastructure at the Hiroshima Synchrotron Radiation Center and assisted with measurements. N.M. and K.I. analyzed (S)ARPES data and wrote the paper with inputs from Y.S., M.S.B., S.I., and Y.M. K.I. conceived and coordinated the research.

Competing interests

The authors declare no competing financial interests.

Corresponding author

Correspondence and requests for materials should be addressed to N. Mitsuishi and K. Ishizaka.

Figures

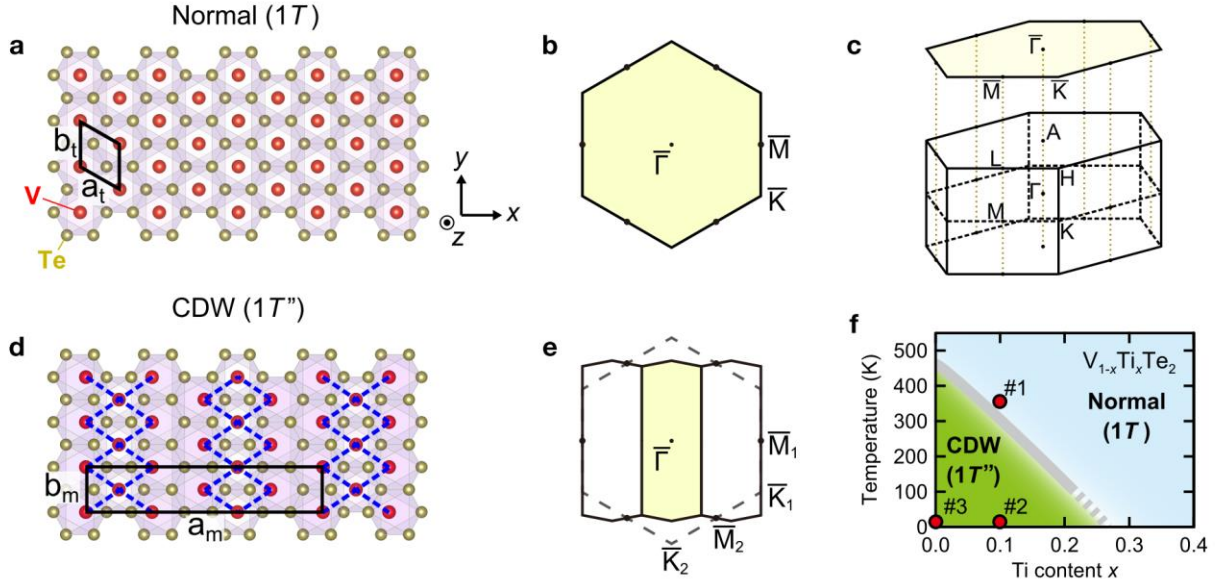


Figure 1 | Normal ($1T$) and CDW ($1T''$) phases in VTe_2 system. **a**, Top view of VTe_2 layer in the high-temperature normal $1T$ phase. The conventional unit cell is indicated by the black lines. **b**, $(0\ 0\ 1)$ surface BZ of $1T$ - VTe_2 . **c**, Bulk BZ of $1T$ - VTe_2 . **d**, Top view of VTe_2 layer in the low-temperature CDW $1T''$ phase. The blue broken lines highlight the shortest V-V bonds forming the double zigzag chains. **e**, $(0\ 0\ 1)$ surface BZ considering the CDW in $1T''$ - VTe_2 , superimposed on that in the $1T$ phase (dashed hexagon). **f**, Schematic electronic phase diagram for $V_{1-x}Ti_xTe_2$, based on the temperature-dependent ARPES measurements.

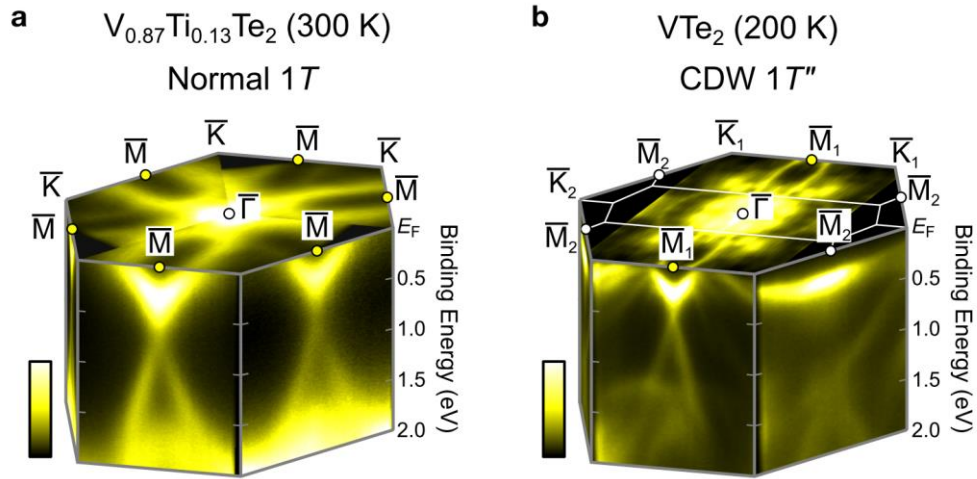


Figure 2 | Overview of Fermi surface and band dispersions for normal 1T and CDW 1T'' phases.
a, Bird's eye ARPES image of 1T- $V_{0.87}Ti_{0.13}Te_2$ (300 K, $h\nu = 21.2$ eV). **b**, Same as a, but for 1T''- VTe_2 (200 K, $h\nu = 90$ eV).

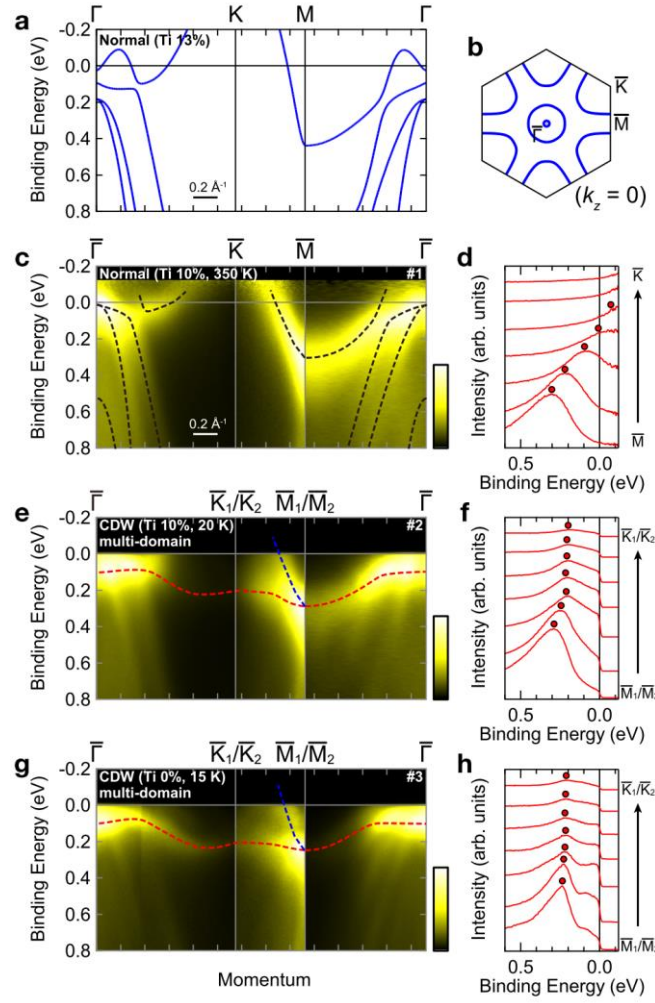


Figure 3 | Temperature/Ti-doping dependence of electronic structures. **a**, The band calculation of $V_{0.87}Ti_{0.13}Te_2$ in normal phase along the high symmetry line (Γ -K-M- Γ). **b**, The corresponding Fermi surface in the $k_z = 0$ plane. **c**, ARPES image of $V_{0.90}Ti_{0.10}Te_2$ in the normal phase (350 K, marked as #1 in Fig. 1f) recorded on the high symmetry lines. The data are divided by the Fermi-Dirac function convoluted with the Gaussian resolution function, to eliminate the thermal broadening of the Fermi cutoff. The broken black curves are the guide for the band dispersions, obtained by tracking the peaks of the energy and momentum distribution curves. **d**, Energy distribution curves along the $\bar{M} - \bar{K}$ line for **c** (integral width: 0.05 \AA^{-1}). **e**, ARPES image of $V_{0.90}Ti_{0.10}Te_2$ in the CDW phase (20 K, #2) for the same momentum region as **c**. The red and blue curves indicate the flat bands and dispersive band near the Fermi level, obtained in a similar manner with **c**. **f**, Same as **d**, but for **e** (#2). **g**, **h**, Same as **e** and **f**, but for the pristine VTe_2 in the CDW phase (15 K, #3). All the ARPES data in the figure were obtained using a He-discharge lamp ($h\nu = 21.2 \text{ eV}$). The data in **e-h** include the signal from all the in-plane 120-degree CDW domains.

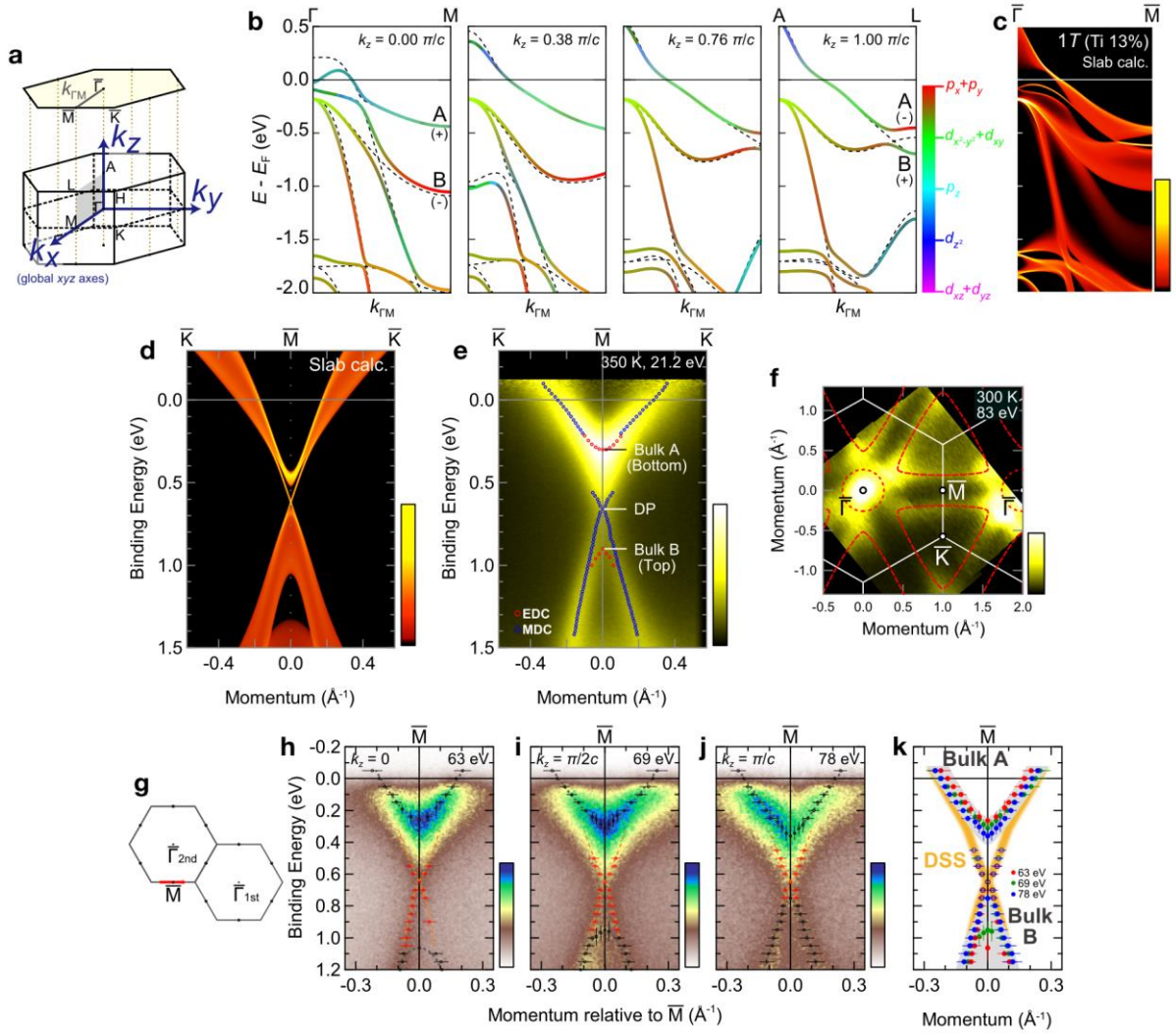


Figure 4 | Topological character of band structures in the normal 1T phase for Ti-doped VTe₂. **a**, The Brillouin zone of 1T phase. k_x , k_y , k_z indicate the axes in the reciprocal space corresponding with the global xyz axes (see Fig. 1a) used for the calculation in **b**. **b**, The bulk band calculations of 1T-V_{0.87}Ti_{0.13}Te₂ along $k_{\Gamma M}$ direction at several k_z values (0, 0.38, 0.76, 1.00 π/c). The color of the curves indicates the weight of orbital characters, as shown by the color-scale. The “+” and “-” mark the even and odd parity, respectively. Broken curves represent the results without spin-orbit coupling. **c**, **d**, The corresponding (0 0 1) slab calculations along the $\bar{\Gamma} - \bar{M}$ (**c**) and the $\bar{K} - \bar{M} - \bar{K}$ (**d**) lines, respectively. **e**, ARPES image of 1T-V_{0.90}Ti_{0.10}Te₂ along the $\bar{K} - \bar{M} - \bar{K}$ direction recorded using a He-discharge lamp (21.2 eV, 350 K). Red (blue) marks represent the peak positions of energy (momentum) distribution curves. **f**, Fermi surface image of 1T-V_{0.87}Ti_{0.13}Te₂ in the $k_z = 0$ plane (circular polarized 83 eV photons, 300 K), with an energy window of ± 5 meV. The red curves display the Fermi surface schematically. **g**, Schematic 2D BZ. The red arrow indicates the measurement region of $h\nu$ -dependent ARPES. **h-j**, $h\nu$ -dependent ARPES measurements of 1T-V_{0.90}Ti_{0.10}Te₂ with 63 eV (**h**), 69 eV (**i**), and 78 eV (**j**) photons (circular polarization, 320 K), which respectively detects at $k_z = 0$,

$\pi/2c$, and π/c plane. Circles with vertical (horizontal) error bars represent the EDC's (MDC's) peak positions. **k**, Schematic band dispersion along $\bar{K} - \bar{M} - \bar{K}$ with experimentally obtained peak plots. The red, green, and blue markers are the peak plots for 63, 69, and 78 eV, respectively from **h**, **i**, and **j**. The orange curve represents the schematic of the Dirac surface state (DSS), whereas the blurred gray curves are the bulk bands (Bulk A and B).

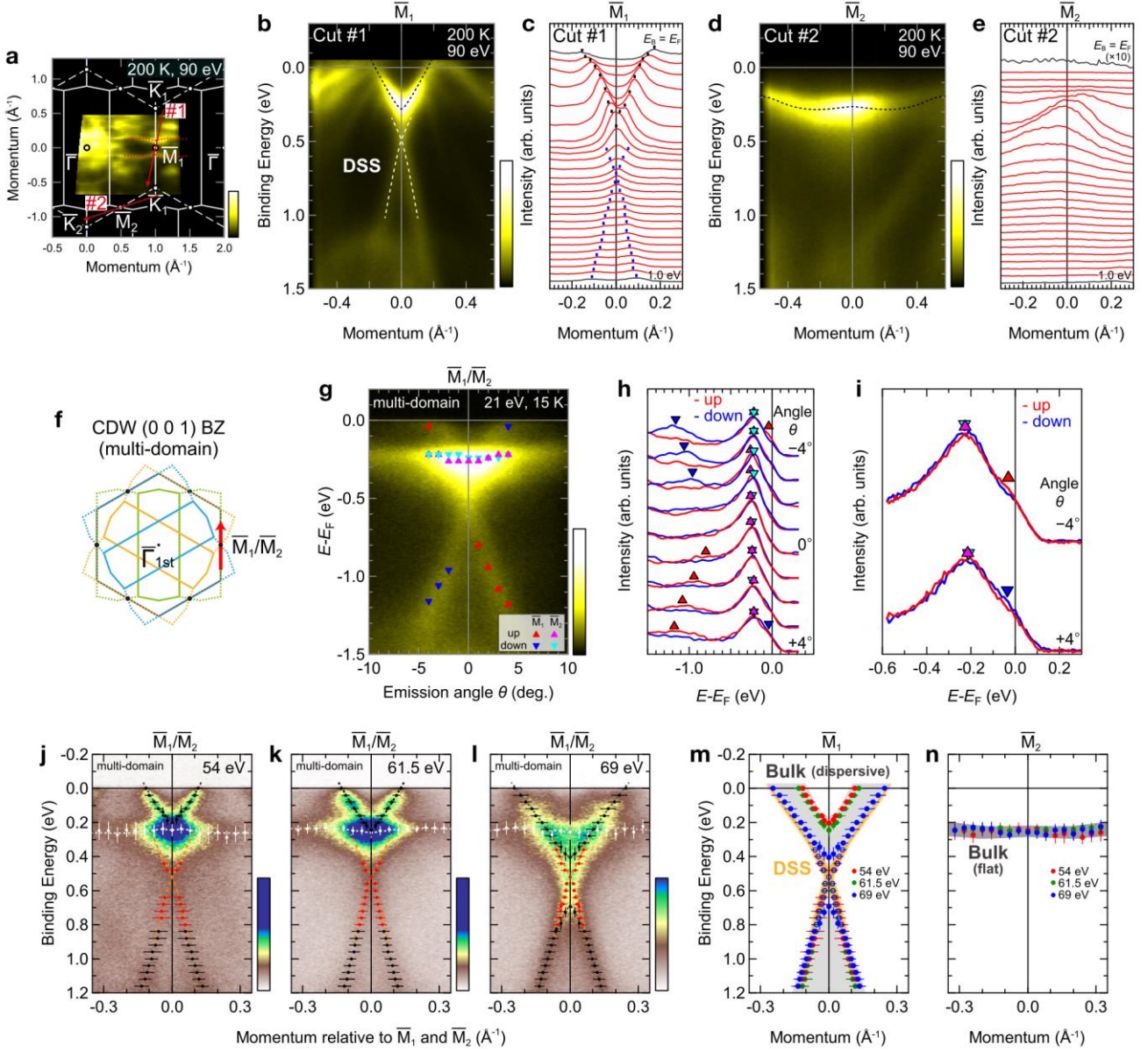


Figure 5 | Anisotropic electronic structures in the CDW 1T'' phase for VTe₂. **a**, Fermi surface image of single-domain VTe₂ recorded with 90 eV photons (circular polarization) at 200 K. White broken lines and full lines indicate the 2D BZ in the 1T and 1T'' phase, respectively. The red dotted curves denote the quasi-one-dimensional Fermi surface peculiar to the 1T'' phase. **b**, ARPES image along cut #1 (as depicted in **a**), roughly along $\bar{K}_1 - \bar{M}_1 - \bar{K}_1$ direction. The black and white dotted curves respectively trace the dispersive bulk band and the Dirac surface state similar to 1T. **c**, MDCs for **b**, ranging from $E_B = 0$ to 1.0 eV (integral width: 0.02 eV). The black (blue) markers represent the MDC peak positions for the dispersive bulk band (Dirac surface state). **d**, ARPES image along cut #2, roughly along $\bar{K}_1 - \bar{M}_2 - \bar{K}_2$ direction. The black dotted curve traces the flat band peculiar to 1T''. **e**, MDCs for **d**. Note that the MDC at the Fermi level is multiplied by 10. **f**, Schematic 2D BZ with mixed in-plane CDW domains. The red arrow qualitatively follows the measurement direction of spin-

resolved and $h\nu$ -dependent ARPES. **g**, ARPES image with the peak plots of spin-resolved spectra (s polarized 21 eV photons, 15 K). The domains are not separated. Red (blue) triangle markers indicate the peak positions of spin-up (-down) spectra of \bar{M}_1 side bands, whereas purple (cyan) for \bar{M}_2 side. **h**, Spin-resolved spectra around \bar{M}_1/\bar{M}_2 points. **i**, Spin-resolved spectra near the Fermi level at $\theta = \pm 4^\circ$. **j-l**, $h\nu$ -dependent ARPES images of a multi-domain sample recorded with 54 eV (**j**), 61.5 eV (**k**), and 69 eV (**l**) photons (s polarization, 15 K). Circles markers with vertical (horizontal) error bars represent the peak positions of EDCs (MDCs). The black and red markers are respectively assigned to the dispersive bulk band and the Dirac surface state at \bar{M}_1 side, while the white markers correspond to the bulk state at the \bar{M}_2 side. **m**, Schematic band dispersion along $\bar{K}_1 - \bar{M}_1 - \bar{K}_1$ with experimental band plots. The red, green, and blue markers are the peak plots for 54, 61.5, and 69 eV, respectively obtained from **j**, **k**, and **l**. The orange curve represents the schematic of the Dirac surface state (DSS), whereas the blurred gray curves are those for the bulk bands. **n**, Same as **m**, but along $\bar{K}_1 - \bar{M}_2 - \bar{K}_2$.

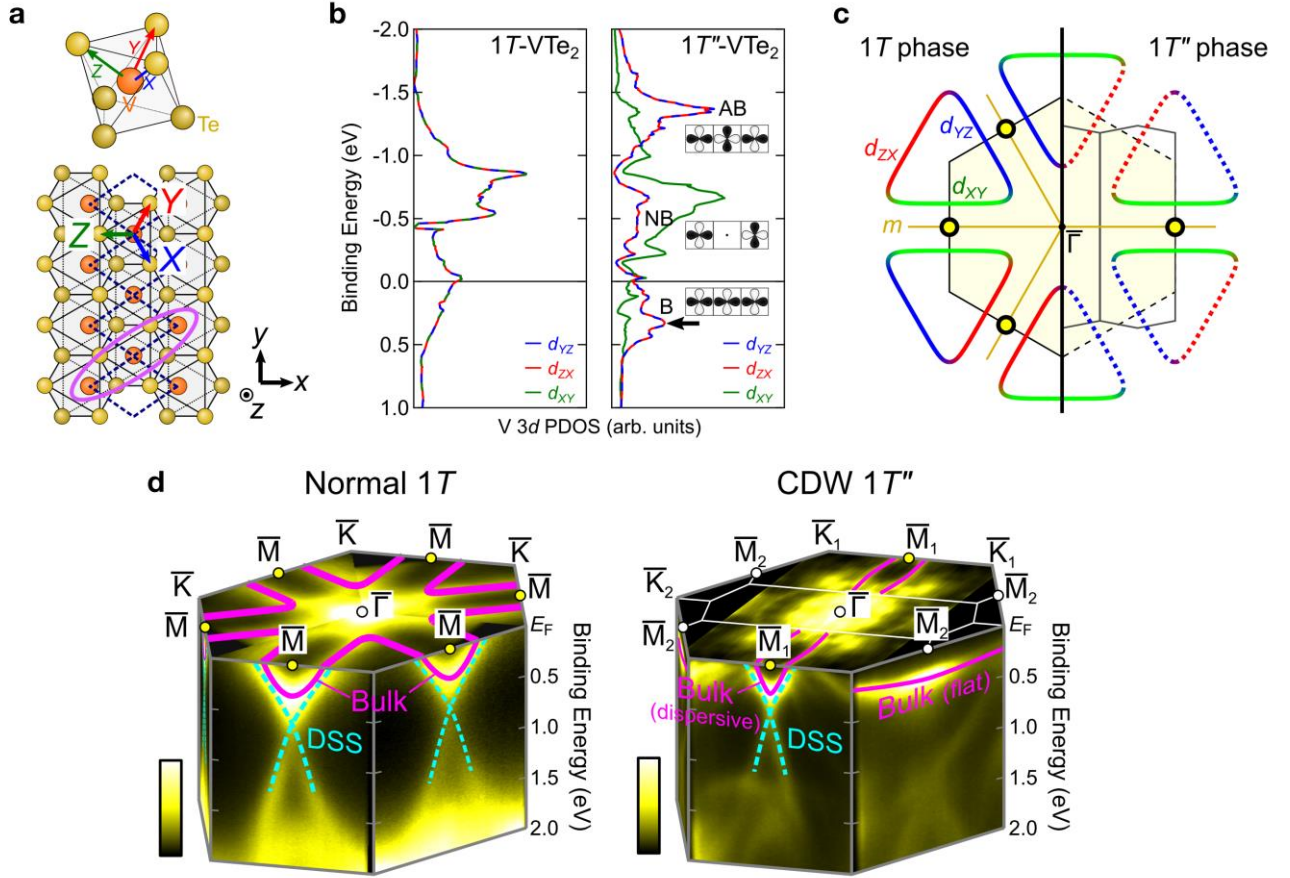


Figure 6 | Strongly orbital dependent electronic modification across the phase transition. **a**, Definition of the local orthogonal coordination (XYZ), set along the VTe_6 octahedron. Here we set Z as the direction perpendicular to the vanadium's double zigzag chains in the CDW $1T''$ phase. The pink oval shows the formation of trimer-like d_{yz} bonding. **b**, Calculated partial density of states (PDOS) for $V3d$ t_{2g} orbitals, d_{xy} , d_{yz} , and d_{zx} . The left (right) panel shows the result for $1T$ ($1T''$) phases. “B”, “NB”, and “AB” indicate the bonding, nonbonding, and antibonding states in $1T''$, respectively, as schematically drawn in the right panel. The black arrow represents the energy position of the flat band. **c**, Schematic drawings of Fermi surfaces around the BZ boundaries, for $1T$ (left) and $1T''$ (right) phases. The color of the curves indicates the orbital characters. The yellow circle markers indicate the location of the Dirac crossing points where the Dirac surface states emerge. The mirror planes are depicted as “ m ”. **d**, Summary of band structures for $1T$ and $1T''$ phases made by the obtained ARPES images ($1T$ - $V_{0.87}Ti_{0.13}Te_2$ (300 K, $h\nu = 21.2$ eV) and $1T''$ - VTe_2 (200 K, $h\nu = 90$ eV)). The purple and dotted cyan curves represent the bulk bands and Dirac surface states, respectively.

Switching of band inversion and topological surface states by charge density wave

Supplementary information

N. Mitsuishi*, Y. Sugita, M. S. Bahramy, M. Kamitani, T. Sonobe, M. Sakano,
T. Shimojima, H. Takahashi, H. Sakai, K. Horiba, H. Kumigashira, K. Taguchi,
K. Miyamoto, T. Okuda, S. Ishiwata, Y. Motome, K. Ishizaka*

Supplementary Note 1: Crystal structure and Brillouin zone of VTe₂.

Supplementary Note 2: Physical properties of V_{1-x}Ti_xTe₂.

Supplementary Note 3: Band calculation of V_{0.87}Ti_{0.13}Te₂ in the normal 1T phase.

Supplementary Note 4: ARPES spectra and EDC/MDC plots along high-symmetry lines.

Supplementary Note 5: Domains in the monoclinic CDW 1T'' phase.

Supplementary Note 6: Temperature-dependent ARPES for V_{0.90}Ti_{0.10}Te₂

Supplementary Note 7: EDCs/MDCs along $\bar{K} - \bar{M} - \bar{K}$ for 1T-V_{0.90}Ti_{0.10}Te₂.

Supplementary Note 8: Setup of spin-resolved ARPES measurement

Supplementary Note 9: ARPES images and EDCs/MDCs along $\bar{K}_1 - \bar{M}_1 - \bar{K}_1/\bar{K}_1 - \bar{M}_2 - \bar{K}_2$ for 1T''-VTe₂.

Supplementary Note 10: Band calculation with V3d orbital weights.

Supplementary Note 11: CDW effects on Te5p orbitals.

Supplementary Note 12: Band unfolding in 1T''-VTe₂.

Supplementary Note 1: Crystal structure and Brillouin zone of VTe₂.

Figures S1a and b respectively show the crystal structure and Brillouin zone of VTe₂ in the normal 1T phase (trigonal, $P\bar{3}m1$). The conventional unit cell is indicated by the black lines (see also Fig. 1 in the main text). Figures S1c and d display the case for the 1T'' phase where the CDW long range order is fully considered (monoclinic, $C2/m$). This CDW exhibits ($3\times 1\times 3$) supercell structure. The superstructure along the stacking direction (*i.e.* the last term “3”) stems from the successive shift of CDWs between the adjacent layers [S1, S2].

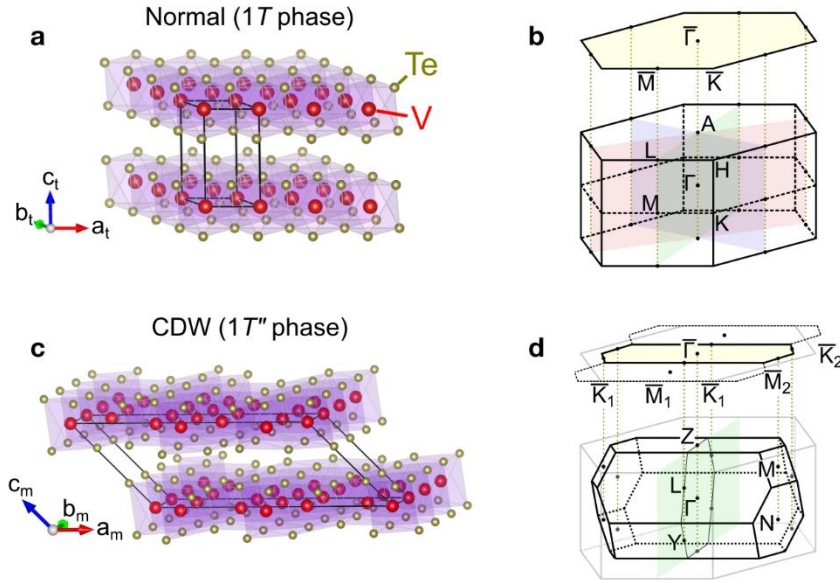


Figure S1 | The details of crystal structure and Brillouin zone of VTe₂. **a**, Crystal structure in the high-temperature normal 1T phase. The conventional unit cell is indicated by the black lines. **b**, (0 0 1) surface 2D and bulk 3D BZs of 1T-VTe₂. Three color (RGB) planes represent the equivalent mirror planes. **c**, Crystal structure in the low-temperature CDW 1T'' phase. **d**, (0 0 1) surface 2D and bulk 3D BZs of 1T''-VTe₂, superimposed on those in the 1T phase (light gray). The green plane indicates the mirror plane.

Supplementary Note 2: Physical properties of $V_{1-x}Ti_xTe_2$.

To grasp the overall phase diagram of $V_{1-x}Ti_xTe_2$, the x -dependent crystal structures and physical properties were thoroughly confirmed by using polycrystalline samples. The polycrystalline $V_{1-x}Ti_xTe_2$ were synthesized by solid state reaction. Stoichiometric mixture of V, Ti and Te powders ($1 - x_n : x_n : 2$) was pelletized and sealed in the evacuated quartz tube. The pellets were heated at 550 °C for 20 hours, and then cooled down to room temperature by furnace cooling. Figure S2a shows the powder x-ray diffraction profiles ($30^\circ \leq 2\theta \leq 33^\circ$) of $V_{1-x_n}Ti_{x_n}Te_2$ at room temperature. Here we note that x_n , the nominal ratio of the raw material powders, does not precisely correspond to the actual x , due to some fluctuation of composition occurring during the growth. For lower x_n compositions, the two peaks assigned to $\bar{6}03$ and 310 reflections with $C2/m$ symmetry are clearly observed, representing the monoclinic $1T''$ phase. With increasing the Ti content, the peaks merge into a single peak corresponding to 101 reflection with $P\bar{3}m1$ structure, thus indicating that the simple trigonal $1T$ structure is obtained. Figure S2b shows the temperature dependence of the electrical resistivity normalized by that at 300 K ($\rho(T)/\rho(300\text{ K})$). With increasing the Ti content, the anomaly corresponding to the phase transition becomes gradually suppressed to the lower temperature region. For $x_n \geq 0.3$, the anomaly is no longer observed in $\rho(T)/\rho(300\text{ K})$, indicating that the normal $1T$ phase becomes stabilized down to the lowest temperature. These results suggest that the $1T-1T''$ transition temperature in this system is favorably controllable by tuning the Ti doping level.

For the ARPES measurements, we synthesized high-quality single crystals of $V_{1-x}Ti_xTe_2$ for $x = 0, 0.10$, and 0.13 , by the chemical vapor transport (CVT) method, as described in Methods. Here, the Ti contents (x) for respective samples were precisely determined by the EDX measurement, to perform the systematic x -dependent study. Figure S2c shows the electrical resistivity for single crystalline $V_{0.90}Ti_{0.10}Te_2$ ($x = 0.10$). The anomaly corresponding to the CDW transition is discerned at around 300 K, which agrees with the temperature-dependent ARPES measurements shown in Supplementary Note 6.

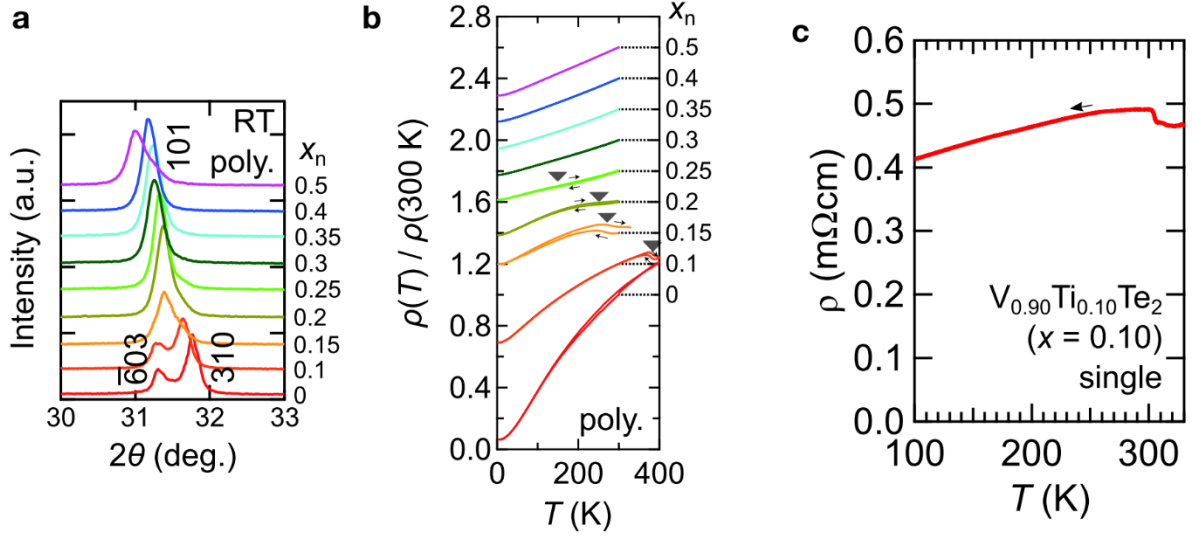


Figure S2 | Physical properties of $V_{1-x}Ti_xTe_2$. **a**, Powder x-ray diffraction profiles recorded at room temperature. Here x_n is the nominal concentration of raw material powders and not precisely same as the actual x value of the grown samples. Miller indices based on the space group $C2/m$ ($\bar{6}03$ and 301) and $P\bar{3}m1$ (101) are depicted. **b**, Temperature dependence of normalized resistivity ($\rho(T)/\rho(300\text{ K})$). The anomaly corresponding to the phase transition are depicted by the gray triangle markers. **c**, Electrical resistivity for single crystalline $V_{0.90}Ti_{0.10}Te_2$ ($x = 0.10$). The anomaly corresponding to the CDW transition is discerned at around 300 K.

Supplementary Note 3: Band calculation of $V_{0.87}Ti_{0.13}Te_2$ in the normal 1T phase.

As discussed in the main text, we have calculated the electronic structure of 1T- $V_{0.87}Ti_{0.13}Te_2$ using virtual crystal approximation method. Figures S3a displays the resulting 3D Fermi surface. Figures S3b-f show orbital-weighted band calculation in the global xyz setting (see also Fig. 4b in the main text).

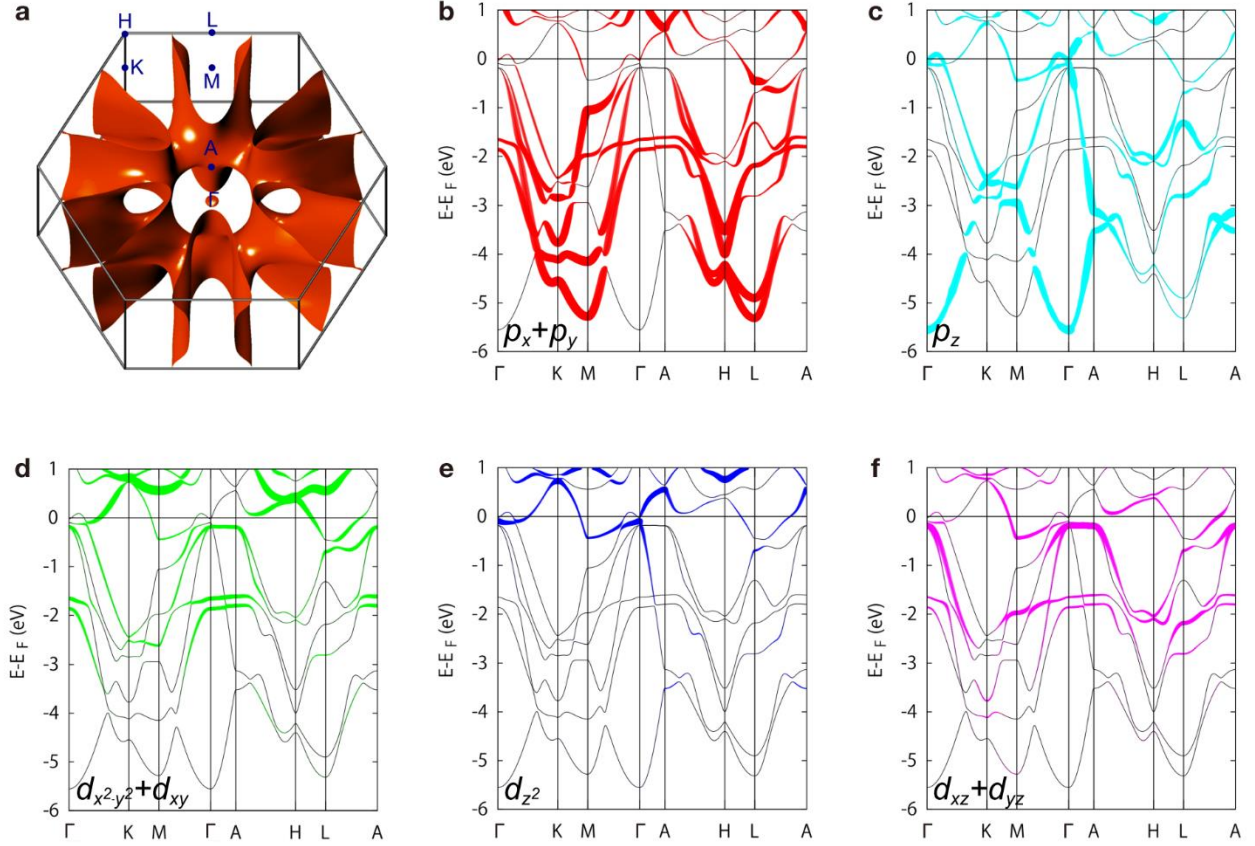


Figure S3 | Calculated electronic structure of 1T- $V_{0.87}Ti_{0.13}Te_2$. a, 3D view of Fermi surface. b-f, Orbital-weighted band dispersions for $p_x + p_y$ (b), p_z (c), $d_{x^2+y^2} + d_{xy}$ (d), d_{z^2} (e), and $d_{xz} + d_{yz}$ (f).

Supplementary Note 4: ARPES spectra and EDC/MDC plots along high-symmetry lines.

Figure S4a, d, and g respectively show the ARPES spectra of $1T$ - $V_{0.90}Ti_{0.10}Te_2$ (350 K), $1T''$ - $V_{0.90}Ti_{0.10}Te_2$ (20 K), and $1T''$ - VTe_2 (15 K), taken with a He discharge lamp ($h\nu = 21.2$ eV), which are identical to Figs. 3c, 3e, and 3g in the main text. The data of Figs. S4a-c are divided by the Fermi-Dirac function convoluted with the Gaussian resolution function, to eliminate the thermal broadening of the Fermi cutoff. Note that the data in CDW phase includes the signal from all domains. The overlaid red (blue) markers indicate the EDC (MDC) peak positions. Figure S3b, e, and h display the corresponding EDCs along $\bar{\Gamma} - \bar{K}$. For $V_{0.90}Ti_{0.10}Te_2$ in normal state, we find no peak structure around the \bar{K} point (see Fig. S4c). On the other hand, for $1T''$ - $V_{0.90}Ti_{0.10}Te_2$ and $1T''$ - VTe_2 , we detect continuous peak structures around $E_B \sim 0.2$ eV, corresponding to the anomalous flat band peculiar to the CDW $1T''$ phase (see also Figs. S4f and i).

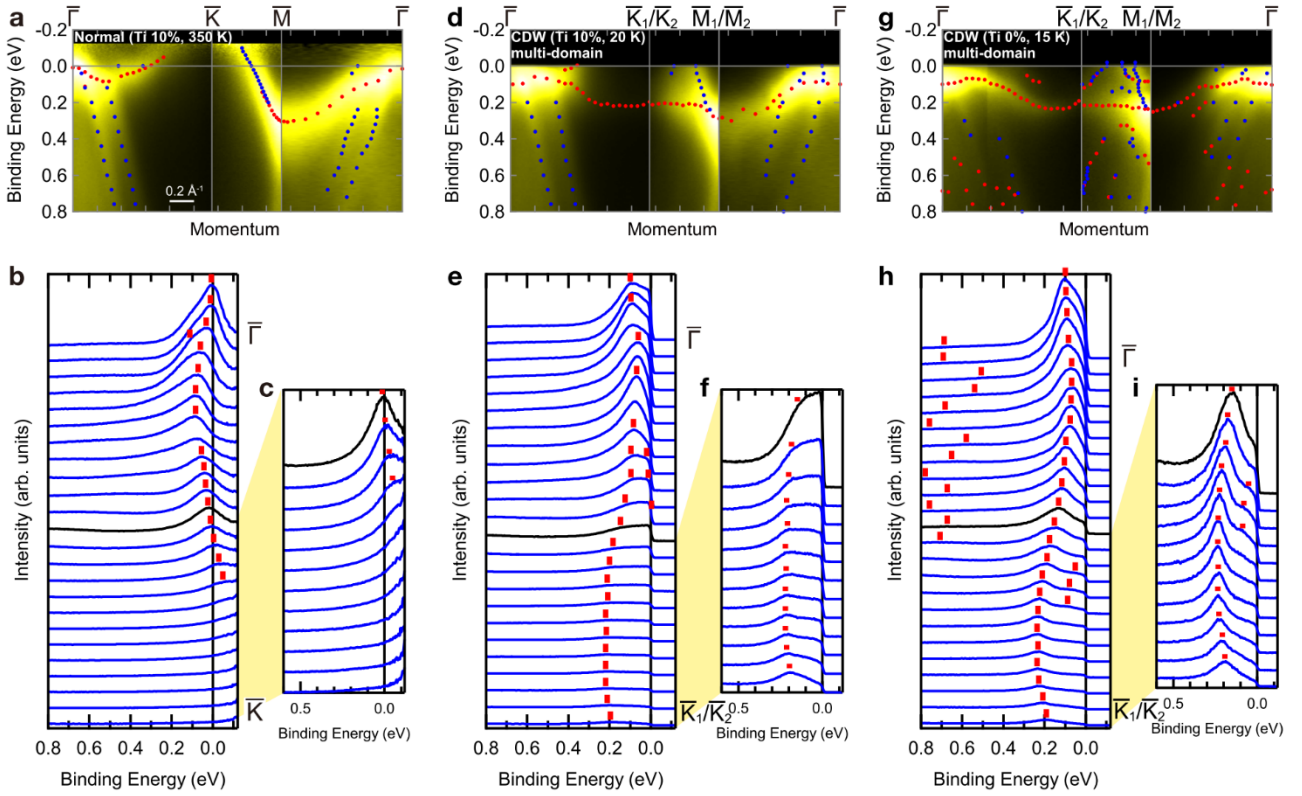


Figure S4 | EDC/MDC plots along the high-symmetry lines with $h\nu = 21.2$ eV. **a**, ARPES image of $1T$ - $V_{0.90}Ti_{0.10}Te_2$ (350 K) with EDC (MDC) peak plots marked by red (blue) circles. **b**, EDCs of **a** along $\bar{\Gamma} - \bar{K}$ (integrated width: 0.05 \AA^{-1}). **c**, Zoom-in of several EDCs around \bar{K} point. The data of **a-c** are divided by the Fermi-Dirac function convoluted with the Gaussian resolution function **d-f**, Same as **a-c**, but for $1T''$ - $V_{0.90}Ti_{0.10}Te_2$ (20 K, multi-domain). **g-i**, Same as **a-c**, but for $1T''$ - VTe_2 (15 K, multi-domain).

Supplementary Note 5: Domains in the monoclinic CDW $1T''$ phase.

In the monoclinic CDW $1T''$ phase, there are six domains in total, due to the mixing of three 120 degree in-plane orientations and two monoclinic tilting orientations [S1]. Figure S5a shows one example of the polarization microscope image of $1T''$ -VTe₂ single crystal with (0 0 1) surface at room temperature. The straight stripes of bright and dark contrast with widths of 10-100 μm confirmed here reflect the domains with two different monoclinic orientations. On the other hand, in some cases, the orientation of the stripe patterns rotating by 120 degrees is observed in the length-scale of 10-1000 μm , as seen in Fig. S5a. From these, we can identify the six domains in the $1T''$ phase. Indeed, the stripe patterns vanish on heating the sample above 475 K, where the normal $1T$ phase is recovered.

The surface structure is also evaluated by a low-energy electron diffraction (LEED) measurement. Figure S5b displays a LEED pattern of $1T''$ -VTe₂ cleaved and taken at room temperature (beam energy: 64 eV). We can assign the observed spots as depicted in Fig. S5c. White circles represent the parent $1T$ spots, whereas red/green/blue circles are (3×1) CDW superstructures of three different in-plane domains. Here no extra spot is detected, thus the surface lattice ordering should be a (3×1) surface unit cell just as expected from its bulk $(3\times 1\times 3)$ superstructure. We also note that similar surface structure is reported in the isostructural NbTe₂ [S2] and TaTe₂ [S3].

In the present ARPES study, the mixing of in-plane 120 degree domains makes it severely difficult to discuss the effect of the zigzag-chain CDW formation. For example, in Figs. 3e-h, the data includes the signal from all the domains since we use a He discharge lamp with the spot size of $\sim 2 \times 2 \text{ mm}^2$. To separately observe the 120-degree domains, we performed ARPES by employing synchrotron radiation with the smaller spot size of $\sim 300 \times 100 \mu\text{m}^2$ (the data shown in Figs. 5a-e).

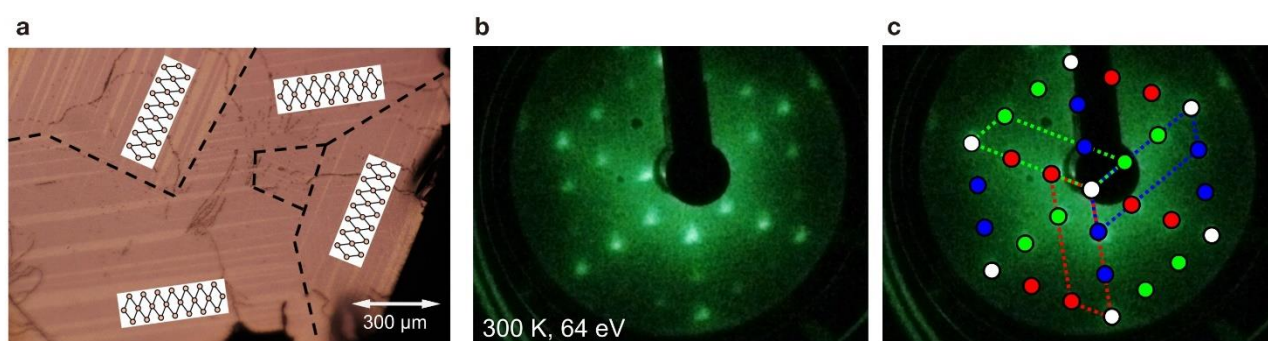


Figure S5 | Domain structure of VTe₂ in the monoclinic CDW phase. **a**, Polarization microscope image at room temperature. 120 degree in-plane domains and their boundaries are respectively depicted by the cartoons and broken lines. **b**, LEED pattern taken with 64 eV beam energy at room temperature. **c**, Spot assignment of **b**. White circles represent the parent $1T$ spots, and red/green/blue circles show (3×1) CDW superstructure of different in-plane domains.

Supplementary Note 6: Temperature-dependent ARPES for $V_{0.90}Ti_{0.10}Te_2$.

We performed temperature-dependent ARPES measurement for Ti-doped $V_{0.90}Ti_{0.10}Te_2$ (transition temperature: ~ 280 K). Figure S6a displays the ARPES image along $\bar{K} - \bar{M} - \bar{K}$, recorded with a He discharge lamp ($h\nu = 21.2$ eV) at several temperatures (cooling process). Note that the data are divided by the Fermi-Dirac function convoluted with the Gaussian resolution function, and in the CDW phase they include the signal from all the in-plane domains. Thus, here we simply use $1T$ notation instead of $1T''$ (e.g. \bar{M} instead of \bar{M}_1/\bar{M}_2). On cooling, the photoelectron intensity reflecting the flat band emerges at around 250 K ($E_B \sim 0.2$ eV), indicating the evolution of CDW. This is also clearly confirmed from the temperature-dependent EDCs at the \bar{K} point (Fig. S6b) and the Fermi momentum (k_F) of the V-shaped bulk band (Fig. S6c). With further cooling, this flat band's peak structure sharpens and increases its intensity. We also note that the near- E_F intensity at k_F in Fig. S6c is gradually suppressed on cooling below the CDW transition. Figures S6d and e show the ARPES images respectively taken at 350 K and 20 K in a wider energy region (Figure S6d is identical to Fig. 4e in the main text). We clearly observe the lower branch of the Dirac surface state at both temperatures.

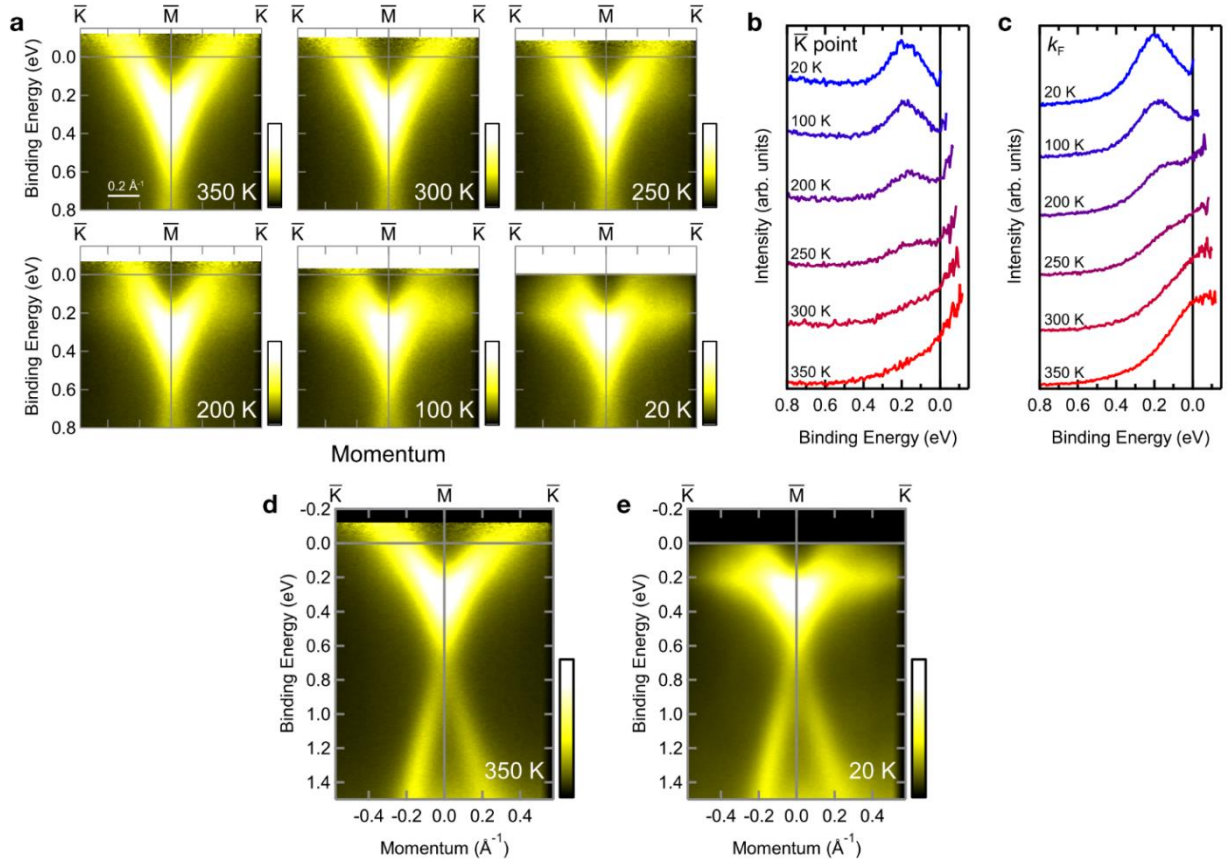


Figure S6 | Temperature-dependent ARPES for $V_{0.90}Ti_{0.10}Te_2$. **a**, ARPES images along $\bar{K} - \bar{M} - \bar{K}$ taken with a He discharge lamp ($h\nu = 21.2$ eV) at several temperatures (350, 300, 250, 200, 100, 20 K). **b**, EDCs of **a** at \bar{K} point. **c**, EDCs of **a** at the Fermi momentum of the V-shaped band. **d**, **e**, ARPES images in a larger energy window taken at 350 K (**d**) and 20 K (**e**).

Supplementary Note 7: EDCs/MDCs along $\bar{K} - \bar{M} - \bar{K}$ for $1T\text{-V}_{0.90}\text{Ti}_{0.10}\text{Te}_2$.

Figure S7 displays EDCs/MDCs with peak plots along $\bar{K} - \bar{M} - \bar{K}$ for $1T\text{-V}_{0.90}\text{Ti}_{0.10}\text{Te}_2$, corresponding to Fig. 4 in the main text. Figures S7a and S7b respectively show EDCs and MDCs taken with a He discharge lamp ($h\nu = 21.2$ eV, 350 K, see Fig. 4e). The energy positions of the bottom of bulk band A ($E_B \sim 0.30$ eV) and the top of bulk band B (~ 0.90 eV) are evaluated from EDCs, and that of the Dirac point (~ 0.66 eV) from MDCs. Figures S7c-h show EDCs and MDCs recorded at 320 K with $h\nu = 63$ (c, d), 61.5 (e, f), and 69 eV (g, h) circular polarization light, respectively corresponding to Figs. 4h, 4i, and 4j in the main text.

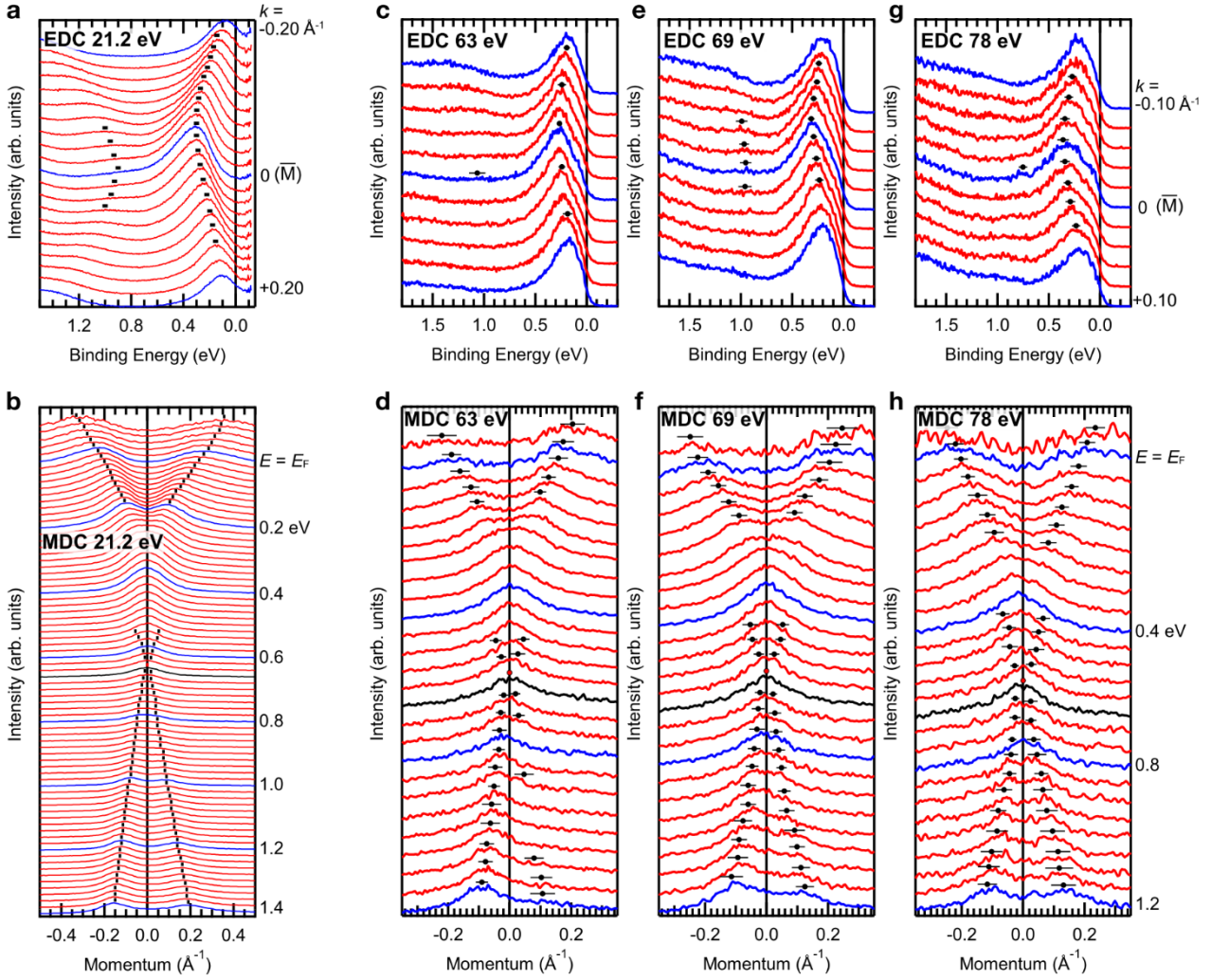


Figure S7 | EDC and MDC of $h\nu$ -dependent ARPES for $1T\text{-V}_{0.90}\text{Ti}_{0.10}\text{Te}_2$. **a, b**, EDCs (**a**) and MDCs (**b**) taken with a He discharge lamp ($h\nu = 21.2$ eV, 350 K). **c-h**, Same as **a** and **b**, but taken at 320 K with $h\nu = 63$ (**c, d**), 69 (**e, f**), and 78 eV (**g, h**) circular polarization light. The markers in the figures denote the peak positions of EDCs/MDCs.

Supplementary Note 8: Setup of spin-resolved ARPES measurement.

Figure S8a shows the geometry of spin-resolved ARPES measurements for multi-domain VTe₂ (see also Methods in the main text). To access the $\bar{K}_1 - \bar{M}_1 - \bar{K}_1/\bar{K}_1 - \bar{M}_2 - \bar{K}_2$ lines, the attached samples are rotated both around the polar (θ) and tilt (φ) axes. Two VLEED spin detectors can be selectively magnetized along (x, z) and (y, z) axes, respectively. The spin detector base (xyz) is converted to the sample base (XYZ) with the rotation matrices:

$$\begin{pmatrix} X \\ Y \\ Z \end{pmatrix} = \begin{pmatrix} 1 & 0 & 0 \\ 0 & \cos \varphi & -\sin \varphi \\ 0 & \sin \varphi & \cos \varphi \end{pmatrix} \begin{pmatrix} \cos \theta & 0 & \sin \theta \\ 0 & 1 & 0 \\ -\sin \theta & 0 & \cos \theta \end{pmatrix} \begin{pmatrix} x \\ y \\ z \end{pmatrix}.$$

The spin polarizations along x, y, z (*i.e.* P_x, P_y, P_z) are obtained by

$$P_{x,y,z} = \frac{1}{S_{\text{eff}}} \frac{I_{x,y,z}^+ - I_{x,y,z}^-}{I_{x,y,z}^+ + I_{x,y,z}^-},$$

where $I_{x,y,z}^+$ ($I_{x,y,z}^-$) is the raw spin-resolved ARPES spectra obtained with the target magnetized in the plus (minus) x, y, z directions. The spin-resolved spectra for spin-up (-down) components along x, y, z directions, $I_{x,y,z}^{\uparrow} (I_{x,y,z}^{\downarrow})$, are obtained by

$$I_{x,y,z}^{\uparrow(\downarrow)} = (1 \pm P_{x,y,z}) \frac{I_{x,y,z}^+ + I_{x,y,z}^-}{2} = (1 \pm P_{x,y,z}) \frac{I_{\text{total}}}{2},$$

where $I_{\text{total}} = I^+ + I^- = I^{\uparrow} + I^{\downarrow}$. The spin polarization and spin-resolved spectra in the XYZ sample base, $P_{X,Y,Z}$ and $I_{X,Y,Z}^{\uparrow(\downarrow)}$, can be obtained by using the following relations,

$$\begin{pmatrix} P_X \\ P_Y \\ P_Z \end{pmatrix} = \begin{pmatrix} 1 & 0 & 0 \\ 0 & \cos \varphi & -\sin \varphi \\ 0 & \sin \varphi & \cos \varphi \end{pmatrix} \begin{pmatrix} \cos \theta & 0 & \sin \theta \\ 0 & 1 & 0 \\ -\sin \theta & 0 & \cos \theta \end{pmatrix} \begin{pmatrix} P_x \\ P_y \\ P_z \end{pmatrix},$$

$$\begin{pmatrix} I_X^{\uparrow(\downarrow)} \\ I_Y^{\uparrow(\downarrow)} \\ I_Z^{\uparrow(\downarrow)} \end{pmatrix} = \frac{I_{\text{total}}}{2} \begin{pmatrix} 1 \\ 1 \\ 1 \end{pmatrix} + \frac{1}{2} \begin{pmatrix} 1 & 0 & 0 \\ 0 & \cos \varphi & -\sin \varphi \\ 0 & \sin \varphi & \cos \varphi \end{pmatrix} \begin{pmatrix} \cos \theta & 0 & \sin \theta \\ 0 & 1 & 0 \\ -\sin \theta & 0 & \cos \theta \end{pmatrix} \begin{pmatrix} I_x^{\uparrow} - I_x^{\downarrow} \\ I_y^{\uparrow} - I_y^{\downarrow} \\ I_z^{\uparrow} - I_z^{\downarrow} \end{pmatrix}.$$

The spin-resolved ARPES data in the main text (Figs. 5g-i) are collected with s polarized 21 eV light at $\varphi = 28^\circ$ and $-4^\circ \leq \theta \leq +4^\circ$ setting. The sample orientation is arranged so that the sample axes X and Y become parallel to the \mathbf{a}_m and \mathbf{b}_m crystal axes for one of the 3 in-plane multi-domain. Figures S8b and c show the raw $I_y^{+(-)}$ spectra and their subtraction ($I_y^+ - I_y^-$) respectively at $\theta = \pm 4^\circ$ (Note that after conversion $I_y^{\uparrow(\downarrow)}$ is displayed in Fig. 5i in the main text). We can find the slight plus/minus contrasts near the Fermi level in these raw data.

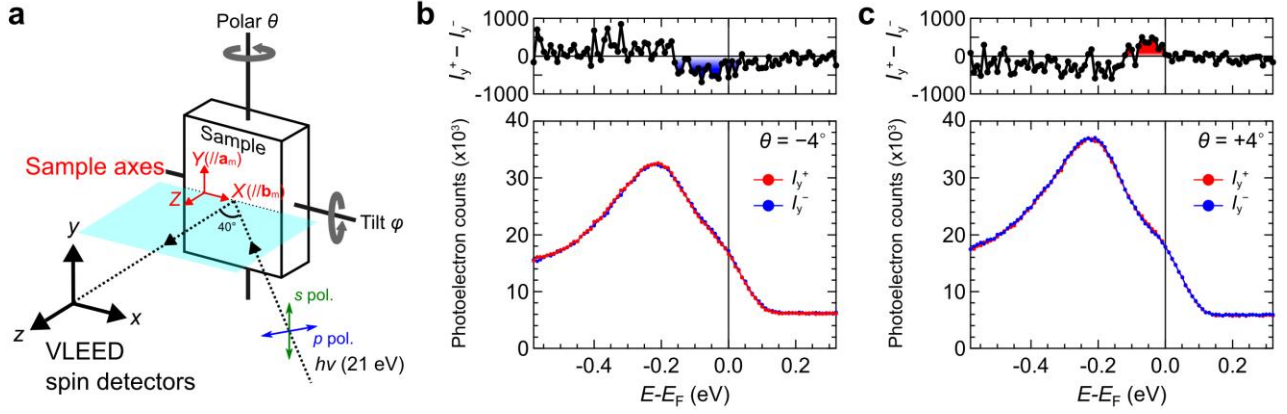


Figure S8 | Experimental setup of spin-resolved ARPES. **a**, Schematic spin-resolved ARPES geometry. The attached samples are rotated around the polar (θ) and tilt (φ) axes to measure the band dispersion along $\bar{K}_1 - \bar{M}_1 - \bar{K}_1/\bar{K}_1 - \bar{M}_2 - \bar{K}_2$. **b**, The raw $I_y^{+(-)}$ spectra and their subtraction ($I_y^{+} - I_y^{-}$) at $\theta = -4^\circ$. **c**, Same as **b**, but at $\theta = +4^\circ$.

Supplementary Note 9:

ARPES images and EDCs/MDCs along $\bar{K}_1 - \bar{M}_1 - \bar{K}_1/\bar{K}_1 - \bar{M}_2 - \bar{K}_2$ for $1T''\text{-VTe}_2$.

The details of ARPES images and their EDCs/MDCs along $\bar{K}_1 - \bar{M}_1 - \bar{K}_1/\bar{K}_1 - \bar{M}_2 - \bar{K}_2$ (15 K, multi-domain) for $1T''\text{-VTe}_2$ are shown in Fig. S9. Figures. S9a, e, i are the data recorded with $h\nu = 54, 61.5, 69$ eV, respectively, which are similarly presented as Figs. 5j, k, l in the main text. Figures S9a, b, and c respectively show the ARPES image, EDCs, and MDCs taken with $h\nu = 54$ eV (s polarized). For a clearer presentation, the MDCs near E_F are again displayed with different offsets in Fig. S9d. The markers in Fig. S9a are obtained by the peaks of EDCs and MDCs shown in Figs. S9b-d. Figures S9e-h and S9i-k similarly shows the sets of results recorded with $h\nu = 61.5$ eV and 69 eV, respectively.

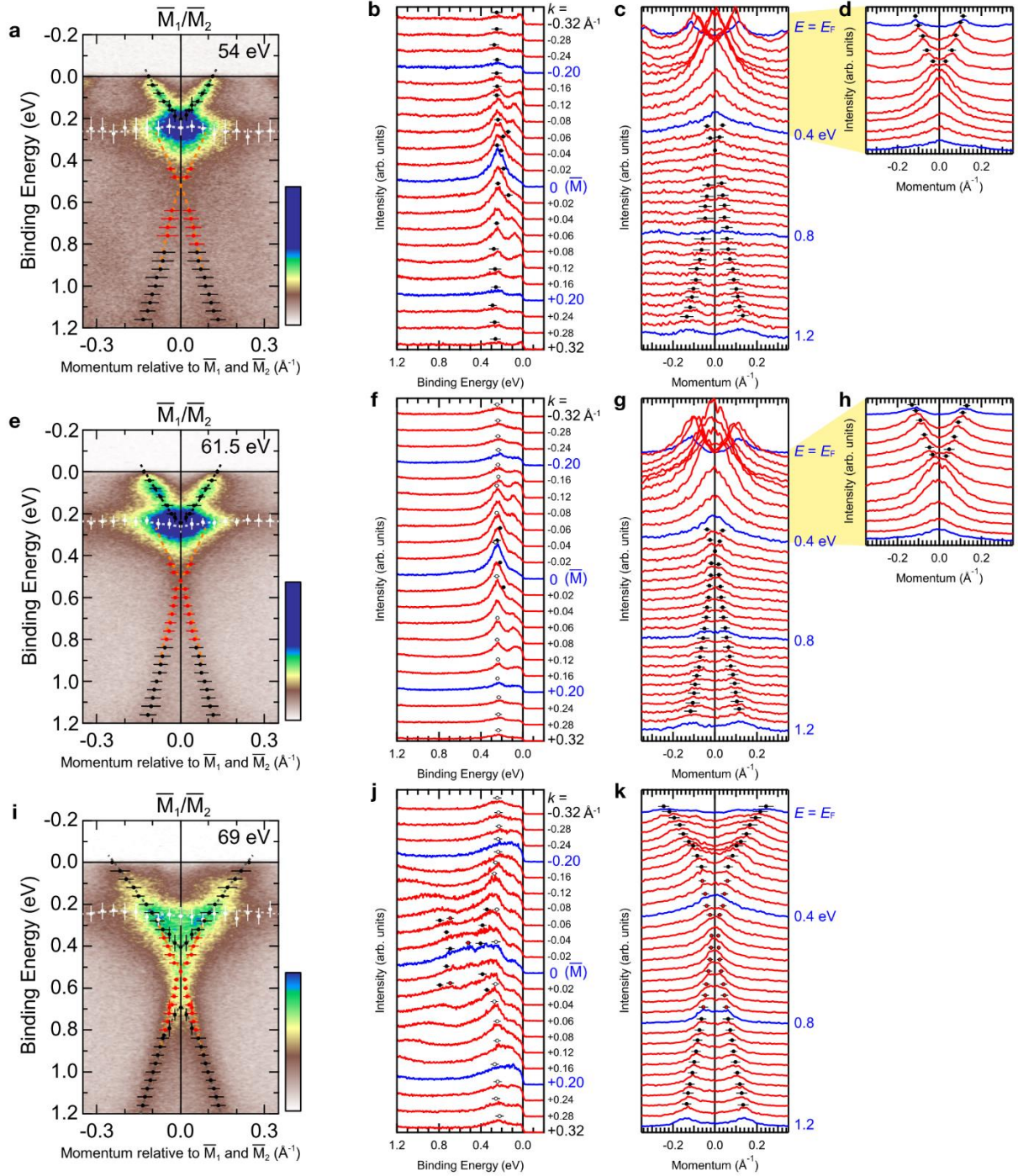


Figure S9 | EDC and MDC of $h\nu$ -dependent ARPES for $1T''$ -VTe₂. **a**, ARPES image recorded with $h\nu = 54$ eV plotted with EDC/MDC peak positions. **b**, EDCs of **a** (integral width: 0.02 \AA^{-1}). **c**, MDCs of **a** (integral width: 0.04 eV). **d**, Zoom-in of several MDCs of **a** around the Fermi level. **e-h**, Same as **a-d**, but taken with $h\nu = 61.5$ eV. **i-k**, Same as **a-c**, but taken with $h\nu = 69$ eV. The markers in the figures denote the peak positions of EDCs/MDCs.

Supplementary Note 10: Band calculation with V3d orbital weights.

Figure S10 shows the V3d-orbital contributions in the electronic band structures of normal (1T) and CDW (1T') VTe₂ obtained by first-principles calculations. The definition of XYZ coordination for *d* orbitals is shown in Fig. 6a in the main text. Figure S10a represents the BZ in the 1T phase; the blue arrows indicate the half-length reciprocal lattice vectors ($\mathbf{a}^*/2$, $\mathbf{b}^*/2$, $\mathbf{c}^*/2$). Figure S10b displays the electronic band structures along the \mathbf{k} path described as the red lines in Fig. S10a. The color and size of circles respectively represent the *d* orbital component and its weight (Note that the small size of circle markers indicate the dominance of Te5*p*). Focusing on the M-K and L-H line, the band crossing the Fermi level is mainly derived from *dx_Y* orbital (green circles). Therefore, by considering the three-fold rotation, each side of the triangular hole Fermi surface surrounding the K point (at $k_z = 0$) consist of one of three V3*d* orbitals, *dy_Z*, *dz_X* and *dx_Y* (see the cartoon of Fermi surfaces in Fig. S10a). Figure S10c shows the total DOS and PDOS for V3*d* and Te5*p*, indicating the dominant contribution of V3*d* in the vicinity of E_F . We note that this calculation of the pristine 1T-VTe₂ predicts stronger V3*d*-Te5*p* hybridization similar to the Ti-doped system V_{0.90}Ti_{0.10}Te₂ (Section S3), thus the topological Dirac surface state is likely to be realized in 1T-VTe₂ as discussed in the main text.

Figures S10d-f show the results for the CDW 1T' phase. For directly comparison with the result for the 1T case, the electronic band structures are plotted along the \mathbf{k} path corresponding to those for the 1T results (see the red lines in Fig. S10d). Looking at the M₁-K₁ line, the band dispersion with the dominant *dx_Y*-orbital contribution cross E_F , which is similar to the 1T case. On the other hand, the flat dispersions with binding energy $E_B \sim 0.4$ eV on the M₂-K₂ line consist of *dy_Z* and *dz_X* orbitals; see also the PDOS in Fig. S10g. As discussed in the main text, we consider that the flat band of *dy_Z*/*dz_X* orbitals originates in the vanadium trimers bonding.

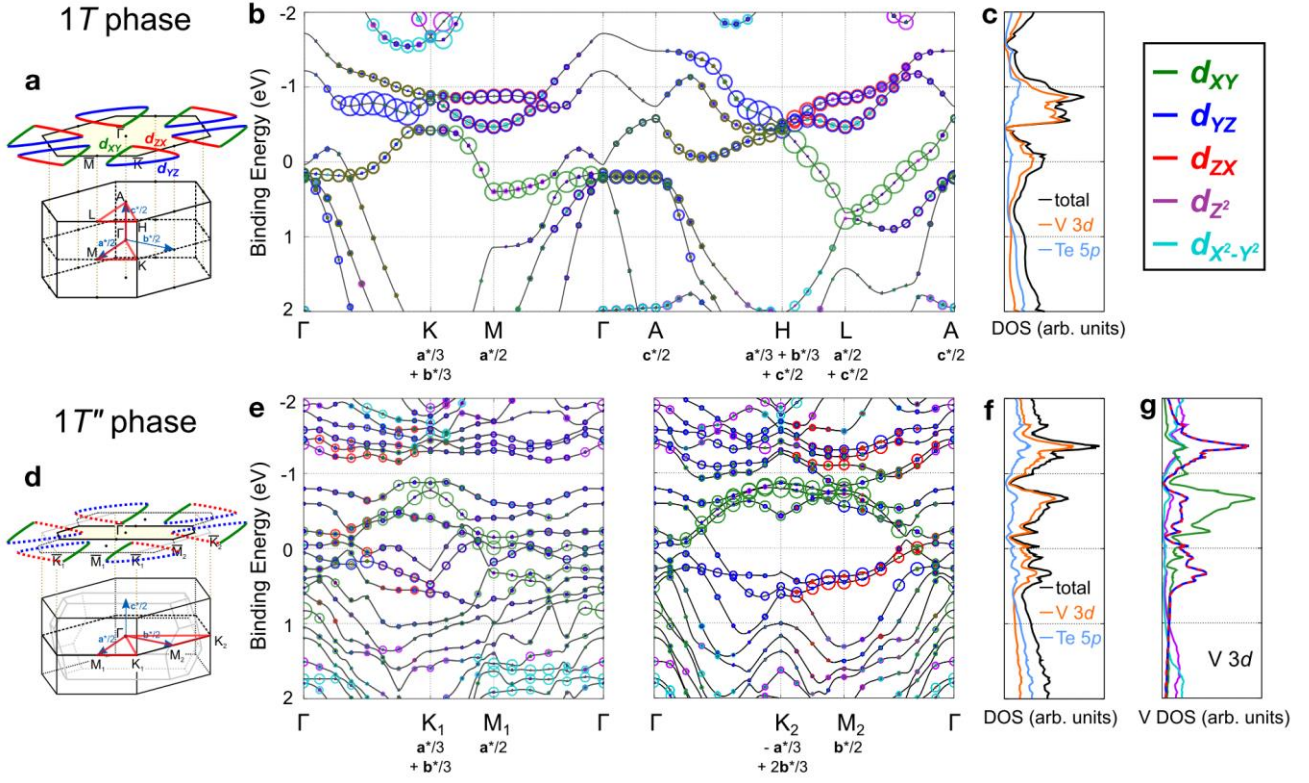


Figure S10 | Electronic band structures of VTe₂ with V3d orbital contributions. **a**, BZ in the normal 1T phase. Cartoons of Fermi surfaces at $k_z = 0$ are also depicted. **b**, Electronic band structures of the 1T phase along the k path indicated by the red lines in **a**. The size and color of the circles indicate the relative weight of each d orbital. **c**, Total DOS and PDOS for V3d and Te5p. **d-f**, Same as **a-c**, but for the CDW 1T'' phase. **g**, PDOS for each V3d orbital in the 1T'' phase.

Supplementary Note 11: CDW effects on Te5p orbitals.

Figure S11a and b show the calculated PDOS of $1T''$ -VTe₂, respectively for V3d (d_{xy} , d_{yz} , d_{zx}) and Te5p (p_x , p_y , p_z). They indicate that the flat band at the binding energy of 0.3 ~ 0.4 eV is formed by the hybridization of d_{yz}/d_{zx} and p_z orbitals. Here we note that d_{yz} and d_{zx} well hybridize with p_z in the edge-sharing VTe₆ octahedral network, whereas the overlap for d_{xy} and p_z is negligibly small (see Fig. S11c).

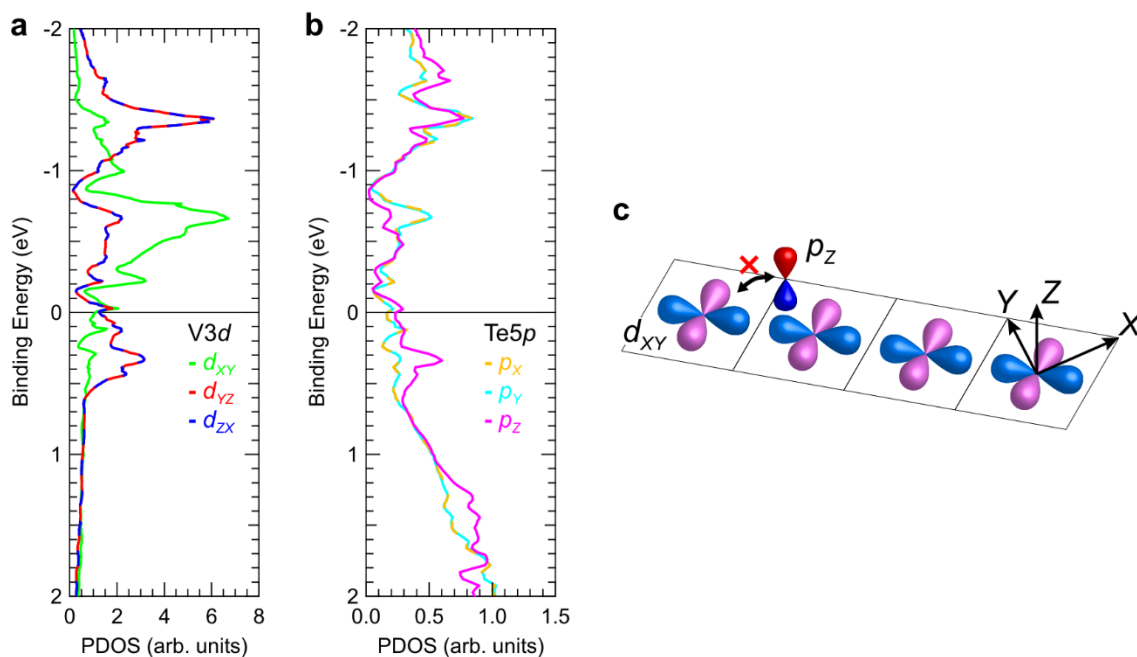


Figure S11 | PDOS of $1T''$ -VTe₂. **a**, PDOS for V3d (d_{xy} , d_{yz} , d_{zx}). **b**, PDOS for Te5p (p_x , p_y , p_z). **c**, Schematic drawing of p_z orbital along with the d_{xy} σ -bonding.

Supplementary Note 12: Band unfolding in $1T''$ -VTe₂.

We have calculated the electronic structures of VTe₂ with the $1T''$ -CDW formation by using the so-called unfolding method, which enables us to directly compare the ARPES results with first principles calculations [S4, S5]. Figures S12b and c show the results along the K_1 - M_1 - K_1 and K_1 - M_2 - K_2 line (see the red and blue arrows in Fig. S12a), which qualitatively reproduce the ARPES results for a single domain region (Figs. 4b and 4d in the main text). We note that the surface state observed in ARPES measurement (Fig. 4b) does not appear in this bulk calculation. Figure S12d displays the constant energy contours obtained by the first-principles calculations (upper panels) and single-domain ARPES measurement (lower panels) at several binding energies (E_B). The both results exhibit the quasi-one-dimensional electronic structure.

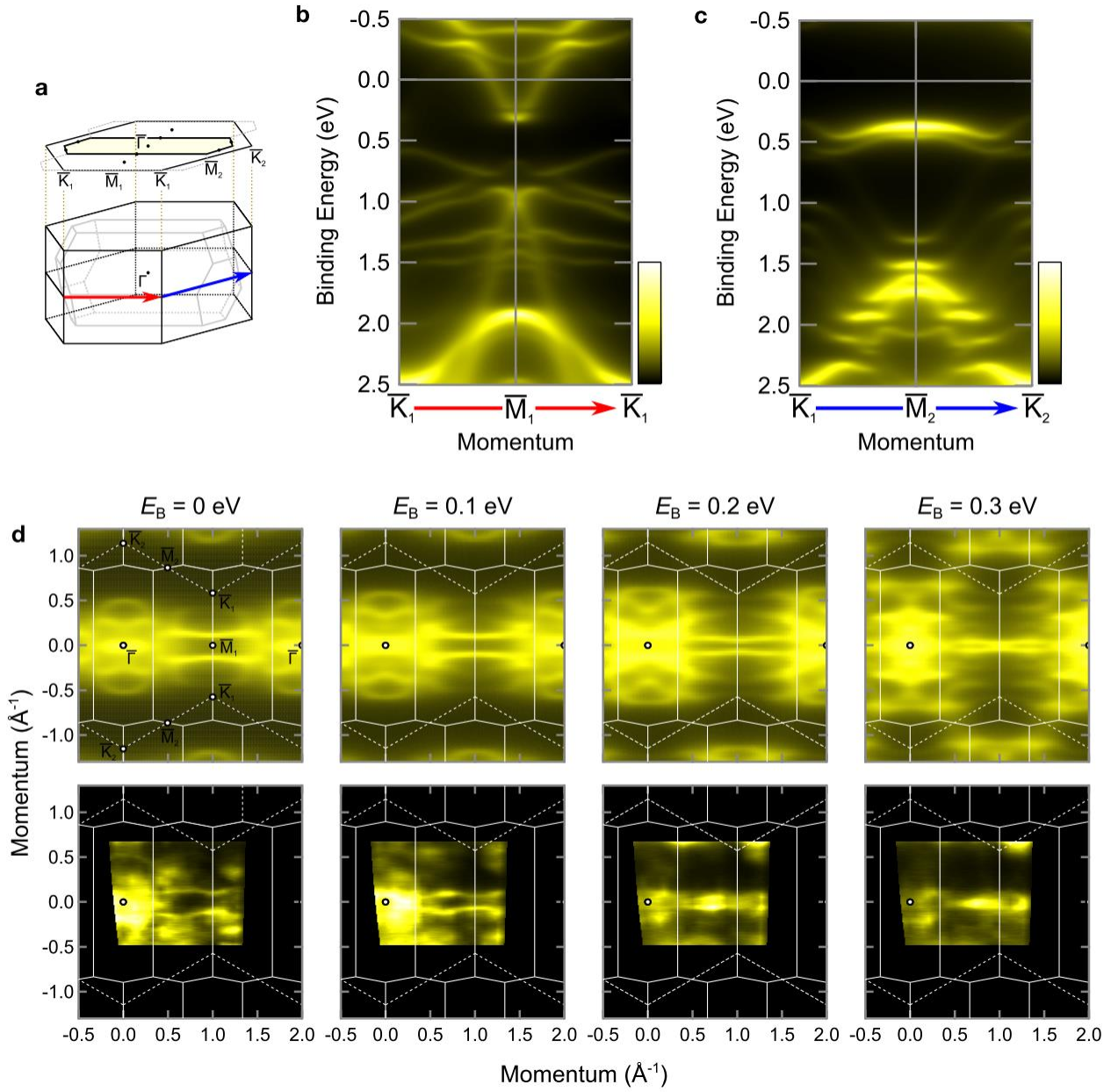


Figure S12 | Calculated electronic structures of $1T''$ -VTe₂ by the unfolding method. **a**, BZ of the normal $1T$ phase (black lines) and the CDW $1T''$ phase (gray lines). **b**, **c**, The calculated band structures along the k paths depicted in **a** by red and blue arrows, respectively. **d**, Constant energy contours obtained by the calculations (upper panels) and experiments (single-domain, lower panels) at $E_B = 0$ (Fermi level), 0.1, 0.2, and 0.3 eV.

Reference

- [S1] Bronsema, K. D., Bus, G. W. & Wiegers, G. A. The crystal structure of vanadium ditelluride, $V_{1+x}Te_2$. *J. Solid State Chem.* **53**, 415–421 (1984).
- [S2] Battaglia, C. *et al.* Fermi-surface-induced lattice distortion in NbTe₂. *Phys. Rev. B* **72**, 195114 (2005).
- [S3] Chen, C. *et al.* Trimer bonding states on the surface of the transition-metal dichalcogenide. *Phys. rev. B* **98**, 195423 (2018).
- [S4] Ku, W., Berlijn, T., & Lee, C.-C. Unfolding First-Principles Band Structures, *Phys. Rev. Lett.* **104**, 216401 (2010).
- [S5] Lee, C.-C., Yamada-Takamura, Y., & Ozaki, T. Unfolding method for first-principles LCAO electronic structure calculations, *J. Phys.: Cond. Matter* **25**, 345501 (2013).